Available online at www.sciencedirect.com
SCIENCE DIRECT®
PERGAMON
International Journal of Heat and Mass Transfer 46 (2003) 4279–4301
International Journal of HEAT and MASS TRANSFER
www.elsevier.com/locate/ijhmt

Analysis of resonances during microwave thawing of slabs

Tanmay Basak *

Department of Chemical Engineering, Indian Institute of Technology, Madras, Chennai 600 036, India

Received 5 June 2002; received in revised form 28 February 2003

Abstract

Resonances or maxima in power absorption due to microwaves incidence within a slab are analyzed via transmitted and reflected waves. A generalized mathematical formulation for uniform plane waves has been established to analyze traveling waves, stationary waves and microwave power absorption within a multiphase sample. Preliminary studies based on the generalized mathematical analysis in ice and water slabs illustrate that greater amplitudes of traveling and stationary waves occur within ice samples, whereas, greater intensity of spatial resonances in microwave power occurs for water samples due to a greater dielectric loss of water. Microwave thawing is studied for specific sample thicknesses which are selected based on greater power distribution within water samples. The enthalpy method is employed for modeling of thawing of ice samples where a superficial mushy region is assumed around the melting point. Depending on the sample thickness, thawing may occur from the unexposed face as well as both the faces when the sample is exposed to microwaves at one face only, whereas thawing may originate from both the center as well as the faces when the sample is exposed to microwaves at both faces. Our analysis based on the generalized mathematical formulation validates the local maxima in spatial power distribution during intermediate thawing stages obtained with the finite element based enthalpy formulation. The generalized mathematical analysis on multiple thawed regimes further illustrates the role of traveling waves on resonances in microwave power. The influence of resonance is attributed by a non-monotonic variation of thawing time with sample thicknesses either for one side incidence or both side incidence due to microwaves. Optimal thawing strategies are recommended based on greater power savings.

Keywords: Microwave; Thawing; Resonances; Phase change; Enthalpy formulation

1. Introduction

Microwaves (MWs) are extensively used for volumetric heating of dielectric materials [1]. Most of the edible materials and salts are dielectric in nature and MWs are often used for heating of frozen materials for a faster processing [2–4]. Efficient MW heating strategies are often practised in industries for a faster processing. During MW heating, the spatial power absorption is dependent on sample geometry, wavelength of MW within the sample medium for a fixed frequency and intensity of radiation [5]. Greater heating effect within a sample is attributed by greater power absorption within a sample. Maxima in power absorption within a sample geometry may enhance local heating characteristics and the maxima in power may be termed as 'resonance'. To investigate the efficient and fast heating procedure, a detailed investigation on the MW power distribution within a sample is needed and resonances may play a significant role to establish the efficient heating strategy. The spatial power distribution and resonances within a sample for uniform plane waves are due to the interference of transmitted and reflected waves within a material. A number of earlier numerical simulations [5,6] was carried out for slabs and cylindrical geometries where resonances, due to constructive interference of propagating waves, were illustrated by the maxima in average power absorbed by the sample. Resonances due to uniform plane waves correspond to a relationship between sample dimensions, wavelength and penetration

* Tel.: +91-44-2257-8216; fax: +91-44-2257-0509.
E-mail address: tanmay@iitm.ac.in (T. Basak).

0017-9310/$ - see front matter © 2003 Elsevier Ltd. All rights reserved.
doi:10.1016/S0017-9310(03)00212-6

Nomenclature

$A_{x,l}$	amplitude of stationary wave lth layer, V m^{-1}
$A^{t}_{x,l}$	amplitude of transmitted wave for lth layer, V m^{-1}
$A^{r}_{x,l}$	amplitude of reflected wave for lth layer, V m^{-1}
Bi	Biot number
C	specific heat capacity, J kg^{-1} K^{-1}
D_p	penetration depth, m
$E_{x,l}$	electric field for lth layer, V m^{-1}
$E^{t}_{x,l}$	electric field due to transmission for lth layer, V m^{-1} (Eq. (3))
$E^{r}_{x,l}$	electric field due to reflection for lth layer, V m^{-1} (Eq. (3))
E_x	electric field intensity, V m^{-1}
E_0	incident electric field intensity, V m^{-1}
f	frequency, Hz
h	heat transfer coefficient, W m^{-2} K^{-1}
H	specific enthalpy, J m^{-3}
I_{OL}	flux of incident radiation from the left face, W m^{-2}
I_{OR}	flux of incident radiation from the right face, W m^{-2}
k	thermal conductivity, W m^{-1} K^{-1}
k	propagation constant
k_0	reference thermal conductivity, W m^{-1} K^{-1}
k_{eff}	effective thermal conductivity, W m^{-1} K^{-1}
L	half-slab thickness, m
q	microwave source term, W m^{-2}
Q	dimensionless microwave source term
s_d	shape factor
t	time, s
T	temperature, K
T_i	initial melting point, K
T_m	melting point, K
T_f	final melting point, K
T_∞	ambient temperature, K
T_0	initial temperature, K
u	dimensionless field component
v	dimensionless real field component
w	dimensionless imaginary field component
z	distance, m
z'	dimensionless distance

Greek symbols

γ	dimensionless propagation constant
ϵ_0	free space permittivity, F m^{-1}
θ	dimensionless temperature
κ'	relative dielectric constant
κ''	relative dielectric loss
κ^*	complex relative dielectric constant
λ	latent heat, J kg^{-1}
λ_m	wavelength in the medium, m
ρ	density, kg m^{-3}
τ	dimensionless time
ϕ_l	liquid volume fraction
$\delta_{x,l}$	phase difference in stationary wave for lth layer
$\delta^{t}_{x,l}$	phase state for transmitted wave for lth layer
$\delta^{r}_{x,l}$	phase state for reflected wave for lth layer
ω	angular frequency, Rad s^{-1}

Subscripts

c	continuous phase
d	dispersed phase
l	liquid phase
l	layer number
s	solid phase

Superscripts

t	transmitted wave
r	reflected wave

depths, whereas resonances are absent for large and small dimensions [6].

During melting or thawing, heating is accompanied by phase change and the sample can be made of liquid, solid and mushy regions. A simultaneous occurrence of multiple phases which include both thawed and unthawed materials, is often observed during volumetric effect due to MWs [3,4,7,8]. Resonances within a multilayered sample during thawing are thus cumbersome due to arbitrary locations of various phase change fronts. The primary focus of this article is to investigate the role of resonances during MW thawing.

A number of experimental observations of resonances has been reported by earlier investigators. Ohlsson and Risman [9] carried out experimental studies on microwave heating at 2450 MHz for spherical and cylindrical samples. Resonances in power absorption were observed at the center of the sample for spheres and cylinders with diameters in the range of 2–6 and 1.8–3.5 cm respectively. Massaudi et al. [10,11] studied the average power absorption in homogeneous and multilayered cylindrical samples by varying the frequency of radiation for a sample with fixed diameter. Their calculations showed the presence of resonances for the multilayered samples only. Ruppin [12] predicted resonance in the average power absorption for cylinders in presence of reflecting surfaces. A greater effect in resonances was observed in spheres. Weil [13] predicted av-

erage power over the frequency range for spheres of radii 3.3 and 6 cm where strong resonances were observed when the frequency was varied. Schundler [14] studied the influence of resonances in power on drying rates of liquid filled spheres. Common to all these experimental studies in enclosed cavities is resonances of power that are primarily functions of the dimension and shape of the cavity and frequency of the incident MW radiation.

A number of theoretical and numerical analysis of resonances of power due to MW heating in slabs and cylinders for uniform plane waves was carried out by earlier investigators [5,6,15]. Barringer et al. [5] studied heating rates and power absorption in cylindrical samples of oil and water. Their modeling studies are based on lumped parameter model of energy balance and the average absorbed MW power, where volumetric spatial power absorption is obtained by solving Maxwell's equations. The resonating effect is more pronounced in water than oil samples. This difference in effect is due to the fact that 3% of the MW power is reflected at an oil–water interface, whereas 64% is reflected at water–air interface. Their model predictions are in good agreement with the experimental studies for a customized oven. Ayappa et al. [6] and Ayappa [15] analyzed resonances in slabs and cylinders for various materials. They established a generalized material invariant relationship between the sample dimension and the wavelength of MWs at a resonating condition. Ayappa [15] analyzed resonances based on stationary waves due to interference of reflection and transmission waves.

The presence of resonances during thawing was investigated by Pangrle et al. [16] and Basak and Ayappa [7]. Pangrle et al. [16] studied thawing of cylindrical samples in presence of radially symmetric MW field and they observed a sharp increase in front velocity at resonating conditions. Basak and Ayappa [7] carried out MW thawing studies for 1D tylose slabs and they found that 2 cm slab thaws faster than 1 cm slab due to resonances when MWs are incident on both sides of the sample. The maxima in average power absorption occurs at the intermediate stages due to presence of multiple thawing fronts. Resonances at the intermediate stages are also observed for thawing of 2D cylinders [4]. To date, a detailed analysis of resonances during MW thawing is yet to appear in the literature.

Here we carry out a detailed analysis of resonance during microwave thawing for 1D ice slabs. MW propagation within a sample is governed by Maxwell's equations whose solution is a linear combination of the traveling waves due to transmission and reflection. A generalized mathematical formulation has been developed to study the influence of traveling waves on resonances of microwave power absorption. MW thawing is studied with the enthalpy formulation based energy balance equation coupled with electric field equations [3,8]. To investigate the influence of resonances at various stages, we study the role of amplitudes and phase states of traveling waves on spatial power distribution, for single and multilayered partially thawed slabs. Based on preliminary investigations for pure samples, we find that the influence of resonance is significant for samples with length scales similar to MWs transport length scales and representative sample thicknesses are selected to illustrate spatial resonances. Our case studies include thawing of samples exposed to MWs at both the faces and one face. Evolution of multiple thawed regimes, interference of waves and resonances of power absorption are studied using our generalized formulation. Optimal thawing strategies are recommended for various sample thicknesses due to MW incidence of fixed frequency and intensity.

2. Theory

2.1. Electromagnetic waves and microwave power: a generalized mathematical formulation

The wave propagation due to uniform electric field E_x is governed by [17]

$$\frac{d^2E_x}{dz^2} + k^2E_x = 0, \tag{1}$$

where E_x lies in x–y plane and varies only along the direction of propagation, z axis (Fig. 1) and $k = (\omega/c)\sqrt{\kappa' + i\kappa''}$, the propagation constant depends on the dielectric constant, κ' and the dielectric loss, κ''. Here $\omega = 2\pi f$, where f is the frequency of the electromagnetic wave and c is the velocity of light. Due to volumetric heating effects, a sample undergoing thawing may consist of multiple layered thawed and unthawed phases

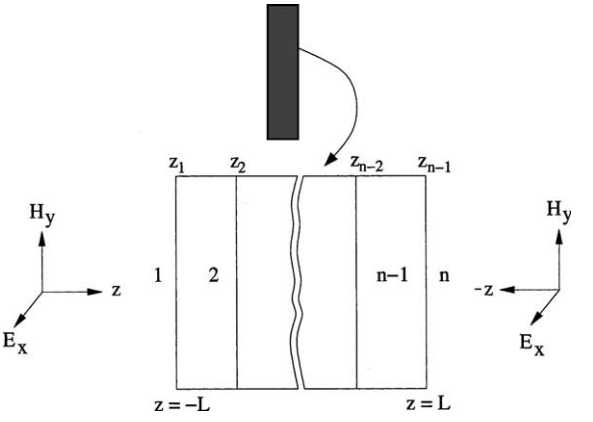

Fig. 1. Schematic illustration of a partially thawed multilayered sample exposed to a plane electromagnetic wave.

[7] as seen in Fig. 1. The electric field in a n multilayered sample for the lth layer obtained from Eq. (1) is

$$\frac{d^2E_{x,l}}{dz^2} + k^2E_{x,l} = 0, \tag{2}$$

where $z_{l-1} \leqslant z \leqslant z_l$ and $l = 1, \ldots, n$. We assume each layer has constant dielectric properties and hence, the general solution to Eq. (2) represented as a linear combination of traveling waves propagating in opposite directions is

$$\begin{aligned} E_{x,1} &= E_{t,1}e^{ik_1z} + E_{r,1}e^{-ik_1z} \quad z = z_1, \\ E_{x,l} &= E_{t,l}e^{ik_lz} + E_{r,l}e^{-ik_lz} \quad z_{l-1} \leqslant z \leqslant z_l,\ l = 2, \ldots, n-1, \\ E_{x,n} &= E_{t,n}e^{ik_nz} + E_{r,n}e^{-ik_nz} \quad z = z_n, \end{aligned} \tag{3}$$

where $E_{t,l}$ and $E_{r,l}$ are the coefficients due to transmission and reflection respectively. The boundary conditions at the interface are

$$\left.\begin{aligned} E_{x,l-1} &= E_{x,l} \\ \frac{dE_{x,l-1}}{dz} &= \frac{dE_{x,l}}{dz} \end{aligned}\right\} \quad \begin{aligned} l &= 2, \ldots, n \\ z &= z_1, \ldots, z_{n-1}. \end{aligned} \tag{4}$$

Using the interface conditions (Eq. (4)) and the general solutions (Eq. (3)), the coefficients, $E_{t,l}$ and $E_{r,l}$ are obtained via solving the set of algebraic equations:

$$\left.\begin{aligned} &E_{t,l}e^{ik_lz_l} + E_{r,l}e^{-ik_lz_l} - E_{t,l+1}e^{ik_{l+1}z_l} - E_{r,l+1}e^{-ik_{l+1}z_l} = 0 \\ &k_lE_{t,l}e^{ik_lz_l} - k_lE_{r,l}e^{-ik_lz_l} - k_{l+1}E_{t,l+1}e^{ik_{l+1}z_l} + k_{l+1}E_{r,l+1}e^{-ik_{l+1}z_l} = 0 \end{aligned}\right\} \quad l = 1, \ldots, n-1. \tag{5}$$

As the incident field intensities from the left and right are known, i.e., $E_{t,1} = E_L$ and $E_{r,n} = E_R$, Eq. (5) are solved for the remaining $2n-2$ coefficients using MATLAB 6.0. For the lth layer, the transmitted and reflected waves are

$$\begin{aligned} E^t_{x,l} &= E_{t,l}e^{ik_lz} = A^t_{x,l}e^{i\delta^t_{x,l}}, \\ E^r_{x,l} &= E_{r,l}e^{ik_lz} = A^r_{x,l}e^{i\delta^r_{x,l}}, \end{aligned} \tag{6}$$

where corresponding amplitudes

$$\begin{aligned} A^t_{x,l} &= \sqrt{E^t_{x,l}E^{t^*}_{x,l}}, \\ A^r_{x,l} &= \sqrt{E^r_{x,l}E^{r^*}_{x,l}} \end{aligned} \tag{7}$$

and the phase states

$$\begin{aligned} \delta^t_{x,l} &= \tan^{-1}\left[\frac{\mathrm{Re}(E^t_{x,l})}{\mathrm{Im}(E^t_{x,l})}\right], \\ \delta^r_{x,l} &= \tan^{-1}\left[\frac{\mathrm{Re}(E^r_{x,l})}{\mathrm{Im}(E^r_{x,l})}\right], \end{aligned} \tag{8}$$

where the superscript, '$*$' in Eq. (7) denotes the complex conjugate. For a stationary wave in the lth layer, the amplitude is

$$A_{x,l} = \sqrt{E_{x,l}E^*_{x,l}} \tag{9}$$

and the difference in phase angle

$$\delta_{x,l} = \delta^t_{x,l} - \delta^r_{x,l}, \tag{10}$$

where the quantities $E_{x,l}$ and $E^*_{x,l}$ appeared in Eq. (9) are evaluated using Eqs. (3) and (6). At the resonance, the difference in phase angle is zero, i.e., $\delta_{x,l} = 0$.

The absorbed power in lth layer, obtained from Poynting vector theorem is

$$q(z) = \tfrac{1}{2}\omega\epsilon_0\kappa''E_{x,l}(z)E^*_{x,l}(z). \tag{11}$$

The average power obtained by integrating the power across the slab is

$$q_{av} = \frac{1}{2L}\int_{-L}^{+L} q(z)dz \approx \frac{1}{2L}\sum_{z=0}^{2L} q(z). \tag{12}$$

The penetration depth D_p and wavelength of radiation in the medium λ_m are related to κ' and κ'' in the following manner:

$$D_p = \frac{c}{\sqrt{2}\pi f\left[\kappa'\left(\sqrt{1+\left(\frac{\kappa''}{\kappa'}\right)^2}-1\right)\right]^{1/2}} \tag{13}$$

and

$$\lambda_m = \frac{c\sqrt{2}}{f\left[\kappa'\left(\sqrt{1+\left(\frac{\kappa''}{\kappa'}\right)^2}+1\right)\right]^{1/2}}. \tag{14}$$

The propagation constant, $k = (2\pi/\lambda_m) + i(1/D_p)$, indicates that λ_m and D_p are the two length scales that determine the electric field distribution within sample. Although generalized length scales for propagation of MWs may be obtained for single phases, for multilayered samples, spatial wave patterns and associated length scales may be quite cumbersome due to spatial dependence of material dielectric properties.

2.2. Modeling of microwave thawing: enthalpy method

In this section, we have analyzed microwave thawing of 1D ice slabs with the enthalpy formulation [8]. The enthalpy formulation is governed by a single energy balance equation with a superficial mushy region as-

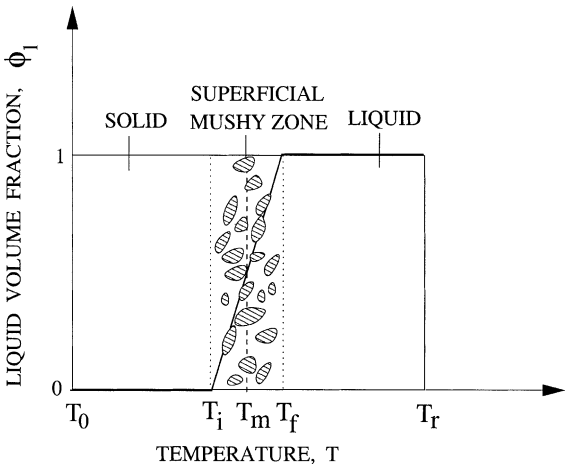

Fig. 2. Schematic illustration of the solid and liquid regions separated by a superficial mushy region. (- - -) the step function for ϕ_l vs T curve at T_m; (—) a linear function for ϕ_l vs T for a superficial mushy region between T_i and T_f. T_0 is the initial temperature of the frozen sample and T_r is a reference temperature within the sample.

sumed to exist around the melting regime (Fig. 2). We assume a local thermal equilibrium between solid and liquid phases. The single energy balance equation based on enthalpy formulation [3,8] for the entire domain is

$$\frac{\partial H}{\partial t} = \frac{\partial}{\partial z}\left(k_{\text{eff}}\frac{\partial T}{\partial z}\right) + q(T), \tag{15}$$

where $q(T)$, defined in a similar manner as in Eq. (11) is the absorbed microwave power, which is a function of temperature during thawing due to the temperature dependency of the dielectric properties as discussed later. Here $k_{\text{eff}} = \phi_l k_l + (1-\phi_l)k_s$ is the effective thermal conductivity with k_l and k_s as thermal conductivities of liquid and solid phases respectively. The total enthalpy, $H(T)$ in Eq. (15) can be written as

$$H(T) = \rho(1-\phi_l)\int_{T_r}^{T} C_s\,d\theta + \rho\phi_l\left[\int_{T_r}^{T_i} C_s\,d\theta + \lambda + \int_{T_i}^{T} C_l\,d\theta\right], \tag{16}$$

where C_l and C_s are the liquid and solid phase heat capacities respectively, λ is the latent heat and ρ is the mean density between the solid and liquid phases. In Eq. (16), T_r represents an arbitrary reference temperature, T_i is the temperature at which phase change initiates, the liquid volume fraction, ϕ_l is in general a function of temperature at a given position in the sample. For pure material, ϕ_l is a step function with a discontinuity at T_m, melting point of the material. In order to implement the enthalpy method, we assume a linear function of ϕ_l for a very small region ($\Delta T = 0.1$ K) around the melting point, T_m as [8]

$$\phi_l = \begin{cases} 0 & T \leqslant T_i, \\ \dfrac{T-T_i}{(T_f-T_i)} & T_i \leqslant T \leqslant T_f, \\ 1 & T \geqslant T_f \end{cases} \tag{17}$$

with $T_i = T_m - \Delta T/2$ and $T_f = T_m + \Delta T/2$. With this assumption, $\phi_l(T)$ reduces to a continuous function removing numerical difficulties associated with a step function (Fig. 2). Hence, for a continuous ϕ_l vs T relationship, a single wave propagation equation for the entire medium obtained from Eq. (1) is

$$\frac{d^2E_x}{dz^2} + k^2(\phi_l)E_x = 0, \tag{18}$$

where $k = (\omega/c)\sqrt{\kappa'(\phi_l) + i\kappa''(\phi_l)}$ is the spatially varying propagation constant. We assume that the dielectric properties are temperature dependent only due to their dependence on ϕ_l. Hence in regions of pure liquid and solid the dielectric properties are assumed to be independent of temperature. The expression for the relative complex dielectric constant $\kappa^* = \kappa' + i\kappa''$ in the mushy zone, based on Fricke's [18] complex conductivity model is

$$\kappa^* = \frac{\kappa_c^*[\kappa_d^*(1+s_dV_d) + \kappa_c^*(1-V_d)s_d]}{[\kappa_c^*(s_d+V_d) + \kappa_d^*(1-V_d)]}, \tag{19}$$

where κ_c^* and κ_d^* are the relative complex dielectric properties of the continuous and dispersed phases respectively, $s_d = 2$ for spherical dispersions and $s_d = 1$ for cylindrical dispersions. V_d the volume fraction of the dispersed phase, is $1-\phi_l$, when the solid is the dispersed phase (liquid continuous) and $V_d = \phi_l$, when liquid is the dispersed phase (solid continuous). Based on our previous analysis [7] we assume solid is dispersed in the continuous liquid phase.

Using the dimensionless variables,

$$u = \frac{E_x}{E_0} \quad \text{and} \quad \frac{d}{dz'} \equiv 2L\frac{d}{dz}.$$

Eq. (18) reduces to

$$\frac{d^2u}{dz'^2} + \gamma^2(\phi_l)u = 0, \tag{20}$$

where u is the electric field intensity, $\gamma(\phi_l) = (2L\omega/c)\sqrt{\kappa'(\phi_l) + i\kappa''(\phi_l)}$ is the propagation constant and $2L$ is the thickness of the slab as shown in Fig. 1. Substituting the complex field variable $u = v + iw$ into Eq. (20) and equating the real and imaginary components, we get

$$\frac{d^2v}{dz'^2} + \chi_1(\phi_l)v - \chi_2(\phi_l)w = 0 \tag{21}$$

and

$$\frac{d^2w}{dz'^2} + \chi_2(\phi_l)v + \chi_1(\phi_l)w = 0 \tag{22}$$

with $\chi_1(\phi_l) = (4L^2\omega^2/c^2)\kappa'(\phi_l)$ and $\chi_2(\phi_l) = (4L^2\omega^2/c^2)\kappa''(\phi_l)$.

For uniform plane waves incident on a sample, some of the radiation is scattered and the rest is absorbed. For 1D slab, boundary conditions [17] for the real and imaginary components are,

$$\left.\begin{aligned}\frac{dv}{dz'} - \frac{2\omega L}{c}w &= \frac{4\omega L}{c}\sin\left(\frac{\omega L}{c}\right)\\ \frac{dw}{dz'} + \frac{2\omega L}{c}v &= \frac{4\omega L}{c}\cos\left(\frac{\omega L}{c}\right)\end{aligned}\right\} \quad \text{at } z' = 0 \tag{23}$$

and

$$\left.\begin{aligned}\frac{dv}{dz'} + \frac{2\omega L}{c}w &= -\frac{E_R}{E_L}\frac{4\omega L}{c}\sin\left(\frac{\omega L}{c}\right)\\ \frac{dw}{dz'} - \frac{2\omega L}{c}v &= -\frac{E_R}{E_L}\frac{4\omega L}{c}\cos\left(\frac{\omega L}{c}\right)\end{aligned}\right\} \quad \text{at } z' = 1. \tag{24}$$

Dimensionless form of the energy balance equation in presence of microwave, Eq. (15), is

$$\frac{\partial \overline{H}}{\partial \tau} = \frac{\partial}{\partial z'}\left(\overline{k}_{\text{eff}}\frac{\partial \theta}{\partial z'}\right) + Q(\phi_l(\theta)), \tag{25}$$

where the expression for the microwave power term in Eq. (25) is,

$$Q(\phi_l(\theta)) = \frac{2L^2\omega\epsilon_0\kappa''(\phi_l)E_0^2}{k_0 T_0}(v^2 + w^2). \tag{26}$$

The initial condition used in the analysis is

$$\theta(\tau = 0) = \frac{T_0 - T_\infty}{T_0} \quad \text{for } 0 \leqslant z' \leqslant 1. \tag{27}$$

In the analysis, Neumann convective boundary condition is used which can be expressed as

$$-\mathbf{n}\cdot\overline{k}_{\text{eff}}\frac{\partial \theta}{\partial z'} = Bi\theta. \tag{28}$$

The coupled energy balance and the electric field equations with the appropriate boundary conditions are solved using Galerkin finite element method in the similar manner as discussed in our previous work [8,19].

3. Results and discussion

3.1. Analysis of MW power distributions in ice and water samples

Preliminary studies have been carried out to analyze the MW power characteristics and resonances for ice and water samples. The dielectric properties are obtained from Table 1. In all cases, the sample is exposed to the MW radiation of intensity 3 $\mathrm{W\,cm^{-2}}$.

In order to study the influence of resonances, the average power, obtained from Eq. (12) is plotted as a function of various sample thicknesses. Fig. 3(a) and (b) illustrate the average power as a function of sample thicknesses where the maxima in average power occurs at $2L/\lambda_m = n$, $0.5n$ [6] for samples with both sides exposed and one side exposed to MWs respectively. The wavelengths, λ_m for ice and water are 6.15 and 1.38 cm respectively, whereas the penetration depths, D_p are 25.81 and 2.76 cm. The average power for ice samples with both sides exposed to MWs incident are greater than that with one side incident cases for all sample thicknesses except for thicker samples (e.g., $2L = 3.2$ cm) as seen in Fig. 3(a). In contrast, the average power for water samples for both sides incident case is lower than that for one side incident case for smaller thicknesses ($2L = 0.7$ and 1.8 cm) at which the local minima in average power occurring due to both side incident case is smaller than the local maxima in average power due to one side incident case. These interesting features as seen in average power vs sample thickness diagram thus provide a suitable guideline in determining the efficient heating route due to MWs incidence. Therefore, it is worthwhile to investigate further the enhanced heating and thawing characteristics for specific sample dimensions.

During intermediate stages of thawing the material may consist of simultaneous solid–liquid phases [7]. As water absorbs greater power than ice as seen in Fig. 3, heating rates in ice–water phases during thawing are greatly influenced by optimal thickness of the water phase. Therefore, to analyze the efficient thawing strategies, we have identified four specific sample thicknesses as $2L = 0.4$, 0.85, 1.5 and 3.2 cm based on greater power absorption in water phases as shown in Fig. 3(b). These specific thicknesses are selected in order to illustrate the significant role of resonance on thawing rate of ice slabs as discussed in later sections.

The maxima in spatial power absorption of the stationary wave is analyzed based on the influence of individual traveling waves due to transmission and reflection. Here we carry out studies on the intensity of spatial resonance of absorbed power for various ice and water samples with amplitudes $(A^t_{x,l}; A^r_{x,l}; A_{x,l})$, and difference between phase angles $(\delta_{x,l})$ where amplitudes and the difference between phase angles are obtained from Eqs. (7)–(10). Figs. 4 and 5 illustrate the amplitudes, difference between phase angles and the MW

Table 1
The thermal and dielectric properties are given for ice (s) and water (l)

Material property	Ice (s)	Water (l)
Heat capacity, C_p ($\mathrm{W\,s\,kg^{-1}\,°C^{-1}}$)	2051	4226
Thermal conductivity, k ($\mathrm{W\,m^{-1}\,°C^{-1}}$)	2.22	0.56
Density, ρ ($\mathrm{kg\,m^{-3}}$)	917	999
Latent heat, λ ($\mathrm{J\,kg^{-1}}$)	3.34×10^5	
Dielectric constant (2450 MHz), κ'	3.95	78.0
Dielectric loss (2450 MHz), κ''	0.3	12.48

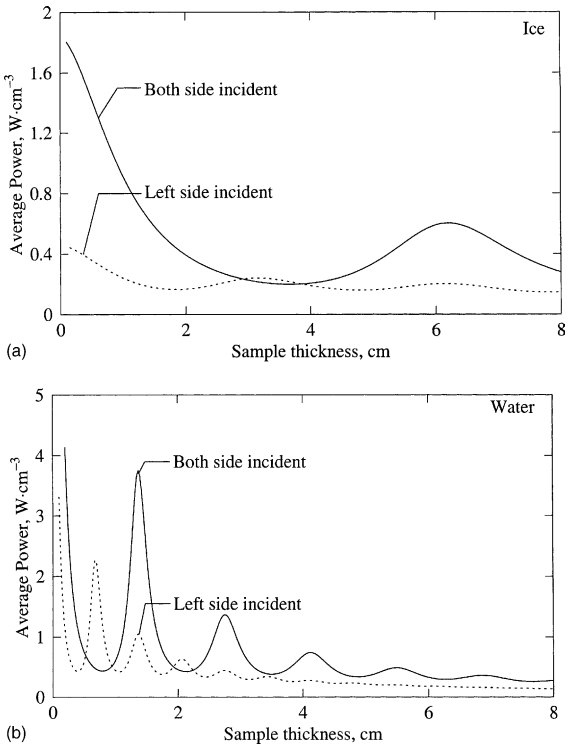

Fig. 3. Average power ($W\,cm^{-3}$) vs sample thickness (cm) for (a) ice and (b) water samples. (—) slabs exposed to microwaves at both faces; (- - -) slabs exposed to microwaves at the left face. $f = 2450$ MHz, for microwaves exposed at both faces; $I_{OL} = I_{OR} = 3\ W\,cm^{-2}$, for microwaves exposed at the left face; $I_{OL} = 3\ W\,cm^{-2}$, $I_{OR} = 0$. Greater maxima in average power occurs for water.

power absorption for ice slabs. As seen in Fig. 4, for all sample thicknesses exposed to MWs at one face, the amplitude of the transmitted wave, $A^{t}_{x,l}$ is greater than that of the reflected wave, $A^{r}_{x,l}$. The amplitude of the stationary electric field has a maxima at the unexposed face for small thicknesses, whereas for the larger sample ($2L = 3.2$ cm) it has two maxima occurring at the faces. The evidence of resonance is illustrated with the difference in phase angles vs positions within a slab. A difference between phase angle of zero illustrates the constructive interference at the unexposed face for smaller samples and at both faces for larger samples. Note that, the phase difference between traveling waves is zero at the resonance which corresponds to a maxima in amplitude of the stationary wave. For all thicknesses, a significant variation of amplitude in stationary electric field corresponds to spatial power absorption ranging between 0.15 and 0.4 $W\,cm^{-3}$.

Fig. 5 illustrates the amplitude and difference in phase angles for ice samples exposed to MWs at both the faces. For all the sample thicknesses, the amplitudes of the transmitted and reflected waves are almost equal. The spatial power is almost uniform for the smaller thicknesses ($2L = 0.4$, 0.85 cm) due to small spatial variation of difference in phase angle which contrast the greater thickness samples where a greater power is deposited at the center. The constructive interference or resonance occurring at the center of the sample is in contrast with one side exposed cases where the resonance occurs either at the unexposed face or both the faces.

Fig. 6 illustrates the amplitudes and differences in phase angles for water samples incident to MWs at one face. For all the samples exposed to MWs at one face as seen in Fig. 6, the amplitude of the transmitted wave is monotonically decreasing function with the distance, whereas the amplitude of the reflected wave is of monotonically increasing order. A resonance for smaller thicknesses ($2L = 0.4$ cm) occurs at the unexposed face due to constructive interference as shown with a zero difference in phase angles (Fig. 6), whereas several resonating zones are seen within a sample with greater thicknesses. For $2L = 0.85$ cm sample, two resonances occur near the exposed and unexposed surfaces. Multiple resonating zones are also found for $2L = 1.5$ and 3.2 cm samples.

Fig. 7 illustrates for water samples exposed both sides to MWs. As the samples are exposed at both the faces, the transmitted and reflected waves are symmetric with each other. For smaller samples ($2L = 0.4$ cm), one resonance is observed at the center, whereas several resonances are observed for greater thicknesses. Although multiple resonances are observed for greater thicknesses, the spatial amplitudes of transmitted and reflected waves are smaller in greater thicknesses for one side and both side incident cases (Figs. 6 and 7). Due to greater penetration of MWs in ice, the maxima in intensity of the traveling and stationary electric fields occurring in ice samples are greater than that in water samples for specific sample dimensions, however the maxima in power absorption is greater in water samples due to greater dielectric loss of water.

3.2. Microwave thawing of ice: case studies

This section analyzes the power and temperature distributions for various thawing intermediates during MW thawing of ice slabs. A constant value of density, 960 $kg\,m^{-3}$ was assumed for both the liquid and solid phases. A uniform initial temperature, $T_0 = 270$ K is used for all slab thicknesses. In all cases an ambient temperature, $T_\infty = 300$ K and a heat transfer coefficient, $h = 2\ W\,m^{-2}\,K^{-1}$ are used. A superficial mushy region of $\Delta T = 0.1$ K is used. The thermal and dielectric properties are given in Table 1. Although the dielectric properties for pure ice and water phases are assumed to be constants, the dielectric properties within the superficial mushy region are the function of temperature (Eq. (19)). For each case, we have used 50 quadratic elements and

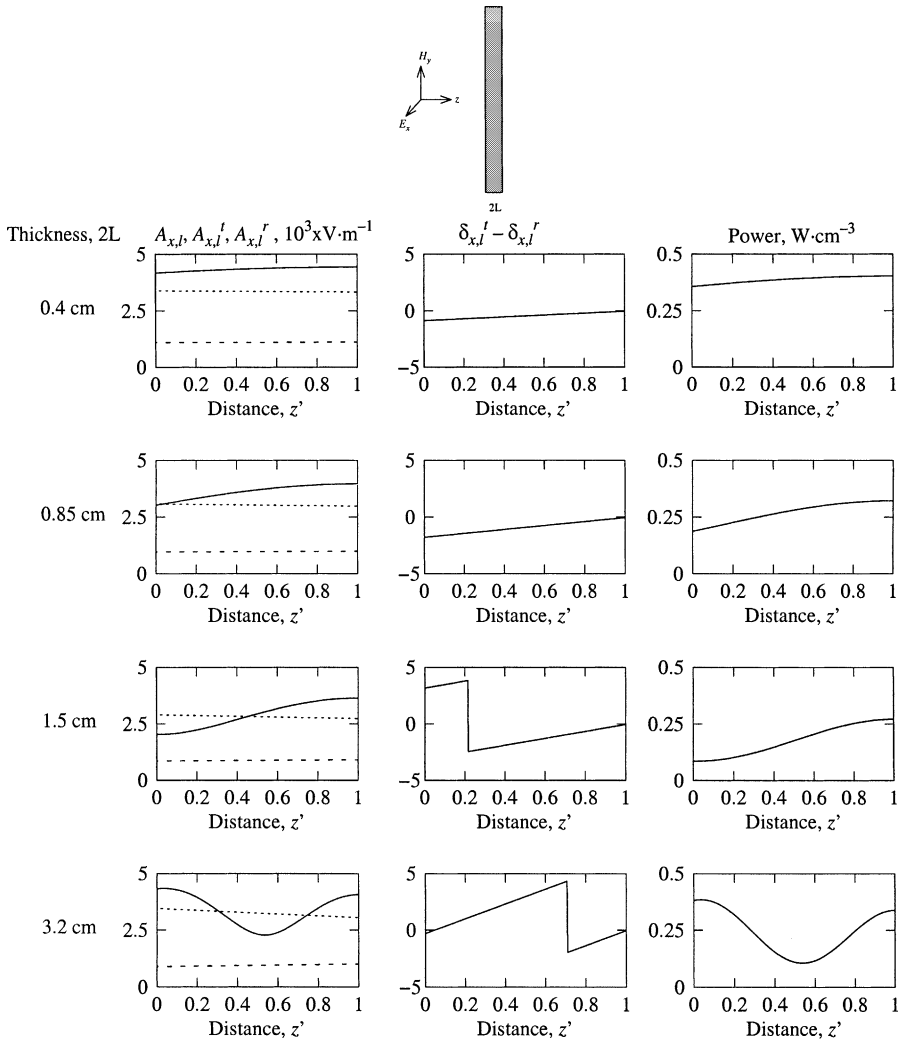

Fig. 4. Amplitudes of electric field $(A_{x,l}, A_{x,l}^{t}, A_{x,l}^{r})$, phase difference $(\delta_{x,l}^{t} - \delta_{x,l}^{r})$ and power distributions for pure ice slabs exposed to microwaves from the left face. $(\cdots)$ transmitted wave; (---) reflected wave; (—) stationary wave. $f = 2450$ MHz, $I_{OL} = 3$ W cm^{-2}, $I_{OR} = 0$. Resonances in power occur at the unexposed face for smaller thicknesses and at both faces for a thicker sample.

the time steps ranging between 0.005 and 0.05 s. Unless stated otherwise, the shaded regions in figures represent the fully thawed regions. The results for microwave heating in a single phase are compared with Ayappa et al. [2] and the results were in excellent agreement (±2%).

3.2.1. Case 1: $2L = 0.4$ cm

Fig. 8 illustrate the thawing characteristics at various thawed regimes for $2L = 0.4$ cm sample exposed to MWs at the left face. Similar to MW heating of pure ice slabs, the maxima in power absorbed is seen at the unexposed face during 1.67 min. During the initial stage the temperature at each point in the sample reaches the initial melting point, $T_i = 272.95$ K, resulting in the entire region becoming mushy, which is however superficial. Due to a greater variation in dielectric loss within this temperature regime, based on Eq. (19), the absorbed power is in general greater than that for pure ice slabs as seen in Fig. 4. At 4.67 min, the power peak is still located at the unexposed face. Consequently, thawing is initiated from the unexposed face of the slab and propagates towards the exposed face with time. A sharp gradient in power is observed near the interface between the unthawed and liquid regimes which also results in a greater variation in temperature as seen in the liquid regime, whereas an almost uniform temperature profile is found within the unthawed/frozen phase. At 7.67 min, the power at the unexposed face is smaller than that during initial stages and a very small amount of power is absorbed in the exposed face. Thawing is completed at 9.85

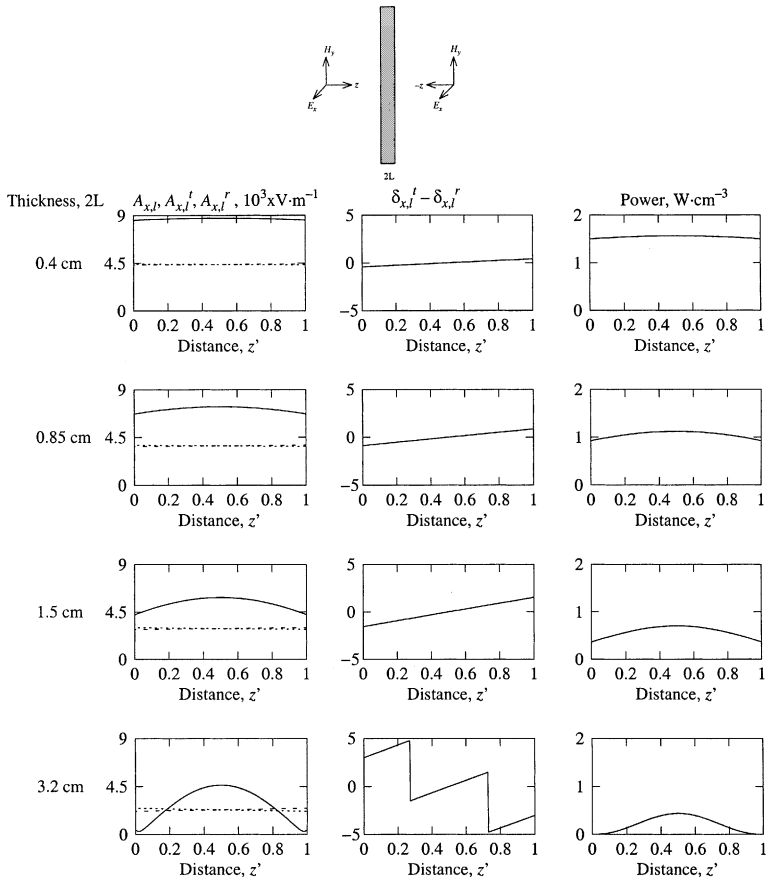

Fig. 5. Amplitudes of electric field $(A_{x,l}, A_{x,l}^{t}, A_{x,l}^{r})$, phase difference $(\delta_{x,l}^{t} - \delta_{x,l}^{r})$ and power distributions for pure ice slabs exposed to microwaves from both faces. $(\cdots)$ transmitted wave; (- - -) reflected wave; (—) stationary wave. $f = 2450$ MHz, $I_{OL} = I_{OR} = 3$ W cm^{-2}. A uniform spatial power absorption occurs for smaller thicknesses and for greater thicknesses, a resonance occurs at the center.

min, where the entire region is liquid and due to a greater dielectric loss an increase in power is observed at the incident face. An interesting feature to note is the smaller absorbed power at the incident face during entire thawing, resulting in a smaller increase in temperature at the incident face when compared with the temperature rise at the unexposed face. Fig. 8(a) illustrates the average power and average temperature distribution with time. A maxima in average power is observed at the initial stage ($t = 1.67$ min) with a greater power at the unexposed face, whereas at the later stages the average power decreases monotonically resulting in a smaller power distribution for the entire sample. The average temperature profile indicates that the heating rates are high during a very early stage of thawing.

Fig. 9 illustrate the thawing characteristics for the sample exposed to MWs at both faces. At the initial stage, the maxima in power absorbed occurs at the center. During 0.67 min, the dielectric properties are strongly dependent on temperature, and hence, a greater power is deposited everywhere at the sample which is in contrast to the pure ice slabs exposed to MWs as seen in Fig. 5. Although the power peak is still located at the center during 2 min, smaller power is deposited in the rest of the sample which contrasts the initial stages ($t = 0.67$ min). Thawing is seen to propagate from the inside out. At 2.33 min, a central liquid layer is formed and a greater temperature distribution is seen within the liquid regime. Due to greater power distribution in presence of MWs exposed to both faces a faster thawing occurs and the entire region is completely thawed in 2.81 min. Common to the left side incident case, a greater thawing rate is found at the initial stages attributed by greater average power and average temperature (Fig. 9(a)).

3.2.2. Case 2: $2L = 0.85$ cm

Fig. 10 illustrate the thawing characteristics for $2L = 0.85$ cm sample exposed to MWs at the left face. Similar to the previous case, the power peak is observed at the unexposed face during an early stage. At 5.67 min, thawing proceeds both from the exposed and unexposed

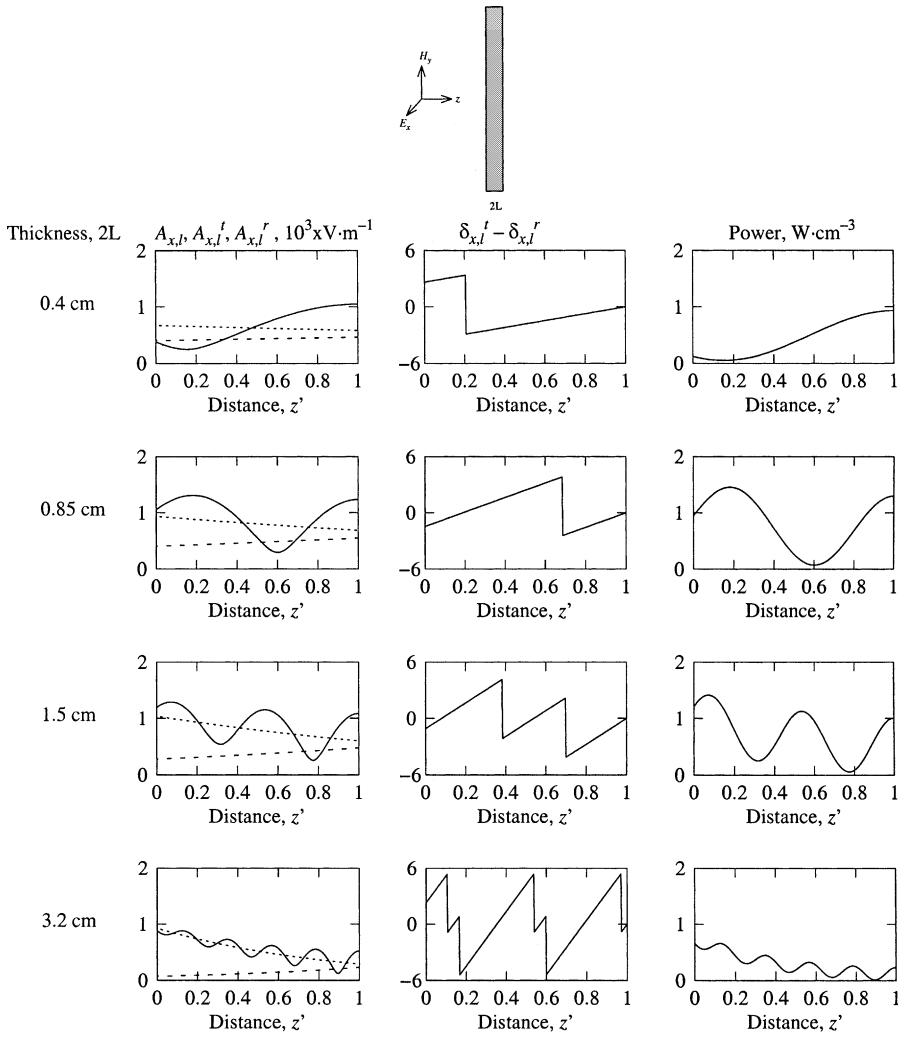

Fig. 6. Amplitudes of electric field $(A_{x,l}, A_{x,l}^{t}, A_{x,l}^{r})$, phase difference $(\delta_{x,l}^{t} - \delta_{x,l}^{r})$ and power distributions for pure water slabs exposed to microwaves from the left face. (···) transmitted wave; (- - -) reflected wave; (—) stationary wave. $f = 2450$ MHz, $I_{OL} = 3$ W cm^{-2}, $I_{OR} = 0$. Resonances occur at the faces for smaller thicknesses, whereas multiple resonances occur for greater thicknesses.

faces of the slab giving rise a central unthawed/frozen phase surrounded by two liquid regimes which contrast the single thawing front propagation for $2L = 0.4$ cm sample as seen in Fig. 8. An interesting feature to note is that during 5.67 min, power rises dramatically at the exposed face, whereas a secondary power maxima is still observed at the unexposed face. Therefore, a greater average power and average temperature are seen at the intermediate stages which result in a greater rate of thawing as observed till 7.33 min. At 7.33 min, almost 85% of the material is thawed. The maxima in average power during the later stages contrast the thawing phenomena for $2L = 0.4$ cm sample resulting in an overall faster thawing rate for $2L = 0.85$ cm slab compared to $2L = 0.4$ cm slab exposed to MWs at the left face only. Note that, $2L = 0.4$ cm slab is completely thawed at 9.85 min, whereas $2L = 0.85$ cm slab takes 8.25 min only.

Fig. 11 illustrate the thawing characteristics for slabs exposed to MWs at both faces. Common to Case 1 (Fig. 9(b); $2L = 0.4$ cm), the thawing front propagates from inside out when slabs are exposed to MWs at both faces. Thawing dynamics may be contrasted for various stages with the dynamics for the slab exposed to MWs at the left face (Fig. 10). The average power distribution shows a maxima at a very early stage and thereafter, the power is monotonically decreasing with time (Fig. 11(a)). Due to greater effect of MWs propagating on both faces, the central thawed regime is observed at 3.33 min, whereas the entire region is unthawed for the slab with the left

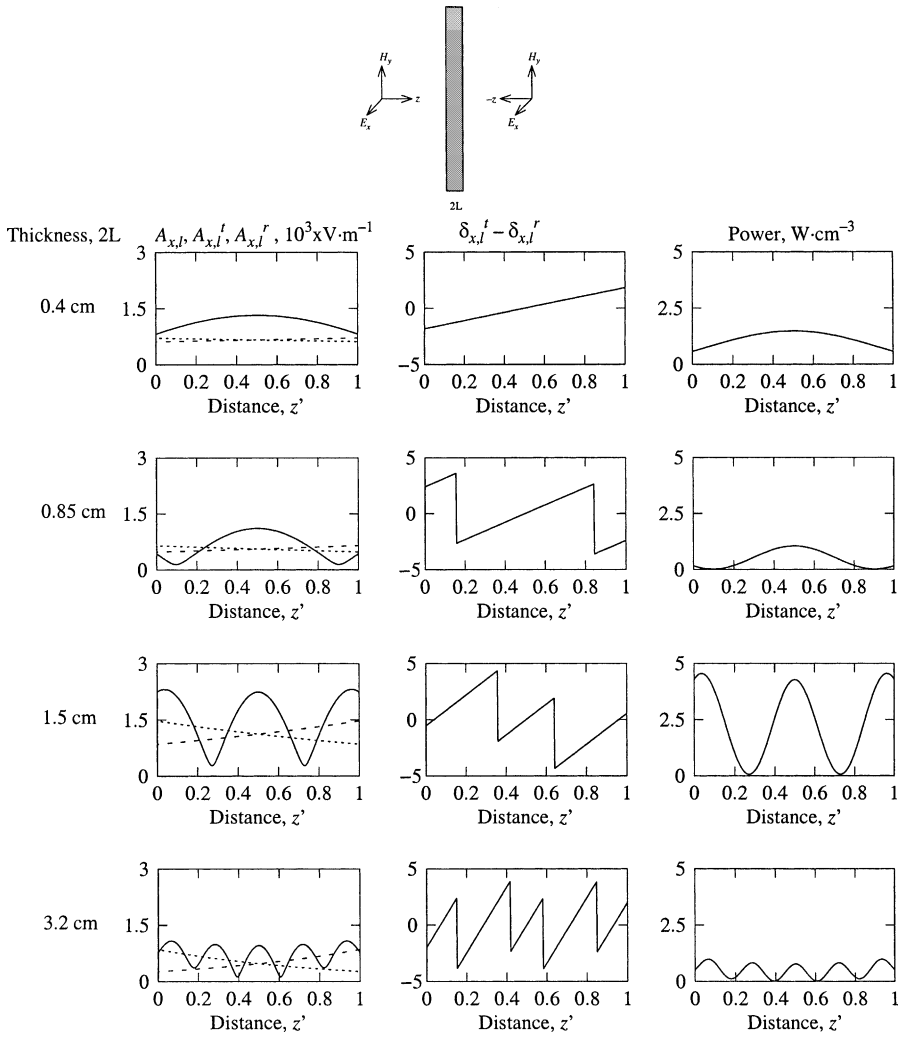

Fig. 7. Amplitudes of electric field $(A_{x,l}, A_{x,l}^{t}, A_{x,l}^{r})$, phase difference $(\delta_{x,l}^{t} - \delta_{x,l}^{r})$ and power distributions for pure water slabs exposed to microwaves from both faces. (···), transmitted wave; (- - -) reflected wave; (—) stationary wave. $f = 2450$ MHz, $I_{OL} = I_{OR} = 3$ W cm^{-2}. Multiple resonances occur for greater thicknesses where the intensity of spatial power absorption is significantly small.

face exposed to MWs during the same time interval as seen in Fig. 10(b). At the intermediate stage, $t = 5.67$ min, 60% of the sample is thawed as seen in Fig. 11(b). During these intermediate stages the average power absorbed is smaller than that for slabs exposed to MWs at the left face and consequently, the slab with both faces exposed to MWs take longer time to thaw. An interesting feature here to note is that the average power vs time plot for $2L = 0.85$ cm slab exposed to MWs at the left face as seen in Fig. 10(a) illustrates the maximum usage of power for a faster thawing.

3.2.3. Case 3: $2L = 1.5$ cm

A few interesting thawing dynamics as seen in Fig. 12 occur for $2L = 1.5$ cm slab exposed to MWs at the left face. Two thawing fronts propagating from both faces are observed at an initial stage, $t = 3.33$ min. A maxima in power is observed near the exposed face resulting in a maxima in average power at the initial stages (Fig. 12(a)). During 10.33 and 14.33 min, a larger thawed regime at the exposed face is seen which is in contrast with the smaller slabs exposed to MWs at the left face where the thawing front propagating from the unexposed face was seen to dominate. The greater power distribution within the thicker thawed region propagating from the exposed face, results in another maxima in average power (Fig. 12(a)). Due to a power deposition during longer period of thawing the average temperature increases rapidly which is also indicated in greater spatial temperature deposition within the thawed regime near the exposed face. At 17 min, thawing is complete; the spatial power deposition is smaller than that during

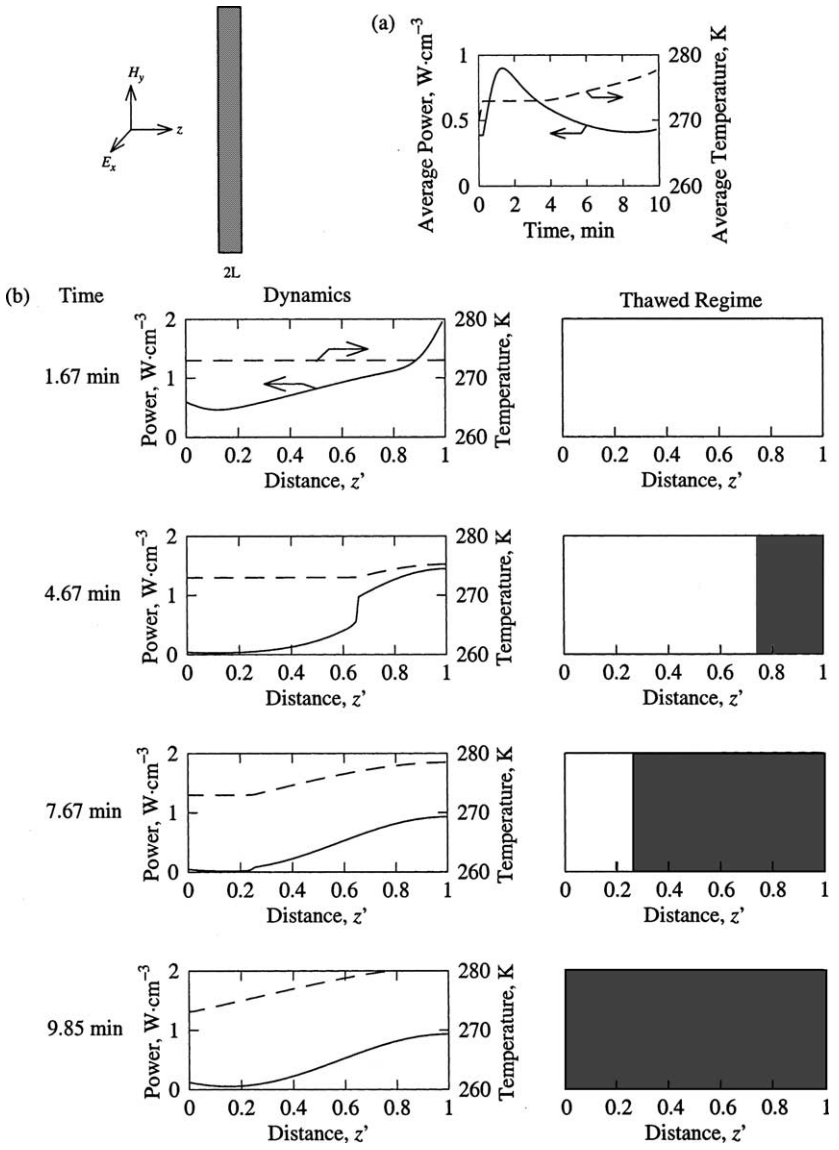

Fig. 8. (a) Average power (—) and average temperature (- - -) vs time; (b) power (—) and temperature (- - -) profiles with thawed regimes (shaded) during microwave thawing of $2L = 0.4$ cm slab exposed to microwaves at the left face. $f = 2450$ MHz, $I_{OL} = 3$ W cm^{-2}, $I_{OR} = 0$. Thawing occurs from the unexposed face and a greater power deposition at the unexposed face is observed during an earlier stage.

the intermediate stages and a hot spot is seen to occur at the exposed face which contrasts the smaller sample with MWs incidence at the left face.

Enhanced thawing rates are observed for the sample exposed to MWs at both the faces as seen in Fig. 13. Similar to the $2L = 0.85$ cm slab exposed to both side (Fig. 11), thawing is seen to propagate from the center. During 5.33 min, a maxima in power, however small, is deposited at the center. At 6.66 min, a thin liquid layer is also formed at the faces where a significantly greater power is absorbed resulting in a maxima in average power distribution. Consequently, the entire thawing process involving the multiple thawing fronts is accelerated and the thawing is complete at 7.57 min. The later stage of thawing is greatly influenced by resonance in power absorption contrasting the thawing dynamics for $2L = 0.85$ cm exposed to MWs at both faces (Fig. 11) where total thawing time is 9.55 min. It is interesting to

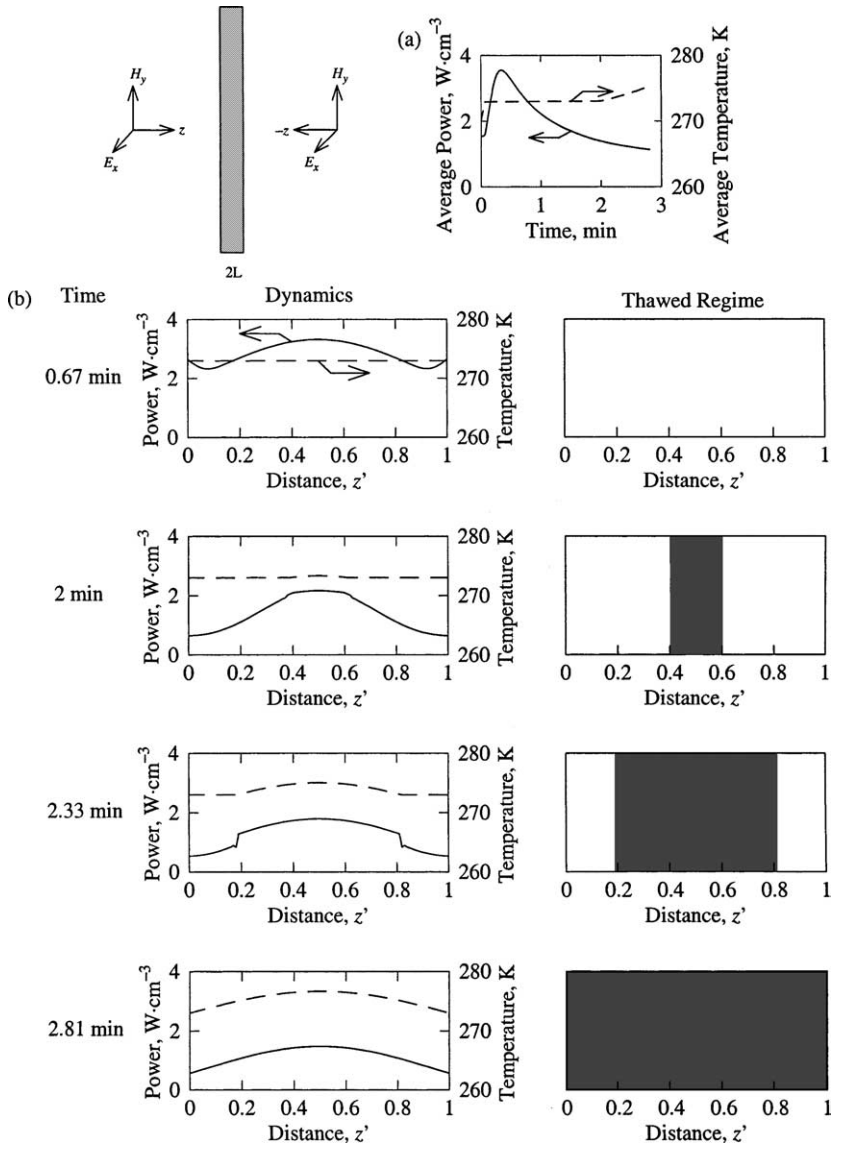

Fig. 9. (a) Average power (—) and average temperature (- - -) vs time; (b) power (—) and temperature (- - -) profiles with thawed regimes (shaded) during microwave thawing of $2L = 0.4$ cm slab exposed to microwaves at both faces. $f = 2450$ MHz, $I_{OL} = I_{OR} = 3$ W cm^{-2}. Thawing is seen to proceed from the center and greater average power is observed at the initial stage.

note that, $2L = 1.5$ cm sample thaws quicker than $2L = 0.85$ cm (when both faces of samples are exposed to MWs).

3.2.4. Case 4: $2L = 3.2$ cm

The thawing process is much longer for greater thicknesses (figures are not shown). Thawing is seen to propagate from the face exposed to MWs which are common for thicker samples based on our earlier studies [7]. Similar to previous cases (Cases 1–3) the maxima in absorbed power always occurs within the liquid regime. During later stages the spatial power shows multiple local maxima as the thawed regime is greater than the wavelength of MWs. Although multiple maxima in average power is observed, the average power distribution is smaller than that for the smaller thicknesses. Thawing rate is approximately doubled for the sample incident at both faces (figures are not shown).

3.3. Analysis of resonances for ice–water phases: representative thawed regimes

In this section, we analyze resonances for some representative cases of various thawed regimes consisting of

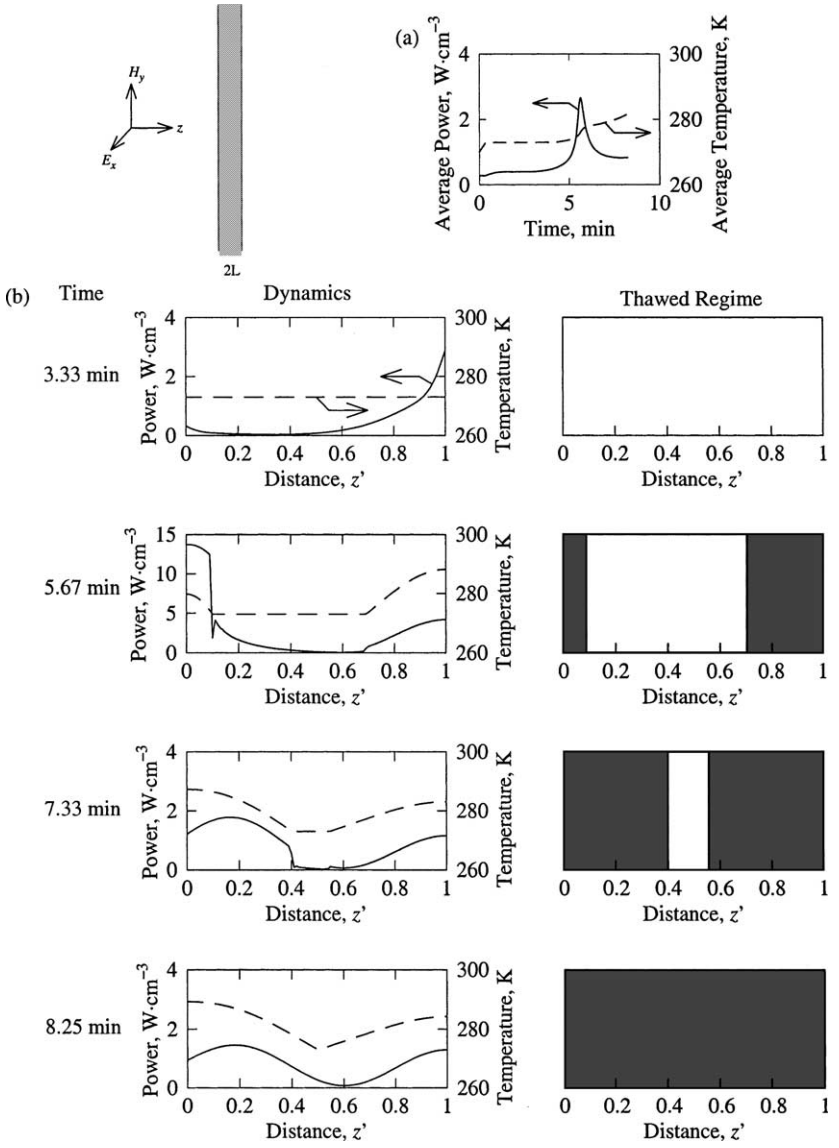

Fig. 10. (a) Average power (—) and average temperature (- - -) vs time; (b) power (—) and temperature (- - -) profiles with thawed regimes (shaded) during microwave thawing of $2L = 0.85$ cm slab exposed to microwaves at the left face. $f = 2450$ MHz, $I_{OL} = 3$ W cm^{-2}, $I_{OR} = 0$. Thawing is seen to proceed from both the faces and greater average power is observed during an intermediate stage.

multiple ice–water phases as seen in earlier section. In order to investigate resonances we have studied the spatial distribution of amplitudes of transmitted and reflected waves, phase states and MW power as obtained from Eqs. (6)–(11) for multilayered ice–water slabs. Figs. 14 and 15 illustrate the spatial distribution of the representative quantities of resonances for four reference sample thicknesses with the shaded region representing the water layer only. The thickness of multilayered ice–water regimes at various stages for each sample thickness is chosen to represent various thawed stages as illustrated in the previous section.

Fig. 14(a)–(c) illustrate the analysis for $2L = 0.4$ cm slab with MW incident at the left face. Fig. 14(a) represents the multilayered slab consisting of a thin layer of water at the face opposite to the MW incidence as illustrated in Fig. 8(b) during an initial stage. The amplitudes of transmitted and reflected waves within the ice region are similar to that of pure ice slab with MW incidence at the left face as illustrated in Fig. 4 and the amplitude sharply changes at the ice–water interface. The resonance in power absorption occurs at the thin layer of water with the difference in phase angle $(\delta_{x,l})$ exactly being zero. It is interesting to note that the

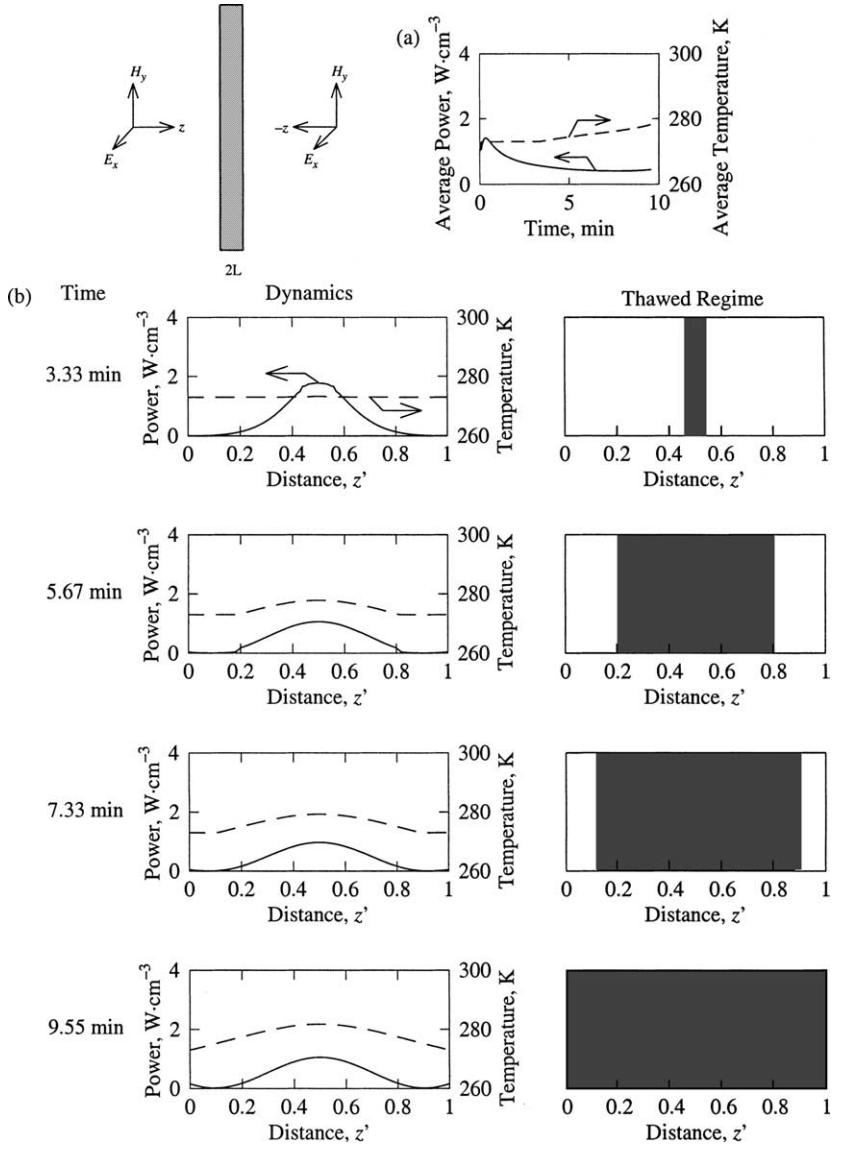

Fig. 11. (a) Average power (—) and average temperature (- - -) vs time; (b) power (—) and temperature (- - -) profiles with thawed regimes (shaded) during microwave thawing of $2L = 0.85$ cm slab exposed to microwaves at both faces. $f = 2450$ MHz, $I_{OL} = I_{OR} = 3$ W cm^{-2}. Thawing is seen to proceed from the center.

sudden jump in spatial power absorption is also observed during the initial stage of MW thawing as illustrated in Fig. 8(b). During an intermediate stage as seen in Fig. 14(b), the amplitude of each traveling wave within the ice layer considerably differs from the initial stage. The role of water thickness at the opposite face seems to play a significant role to change the spatial pattern of traveling waves within the ice layer where the amplitude of the transmitted wave is seen to be decreased and that for reflected wave increased. The amplitude of the stationary wave within the ice layer is smaller than that at the initial stage and the smaller amplitude is due to a greater destructive interference in presence of a water layer near the unexposed face. The smaller MW power deposition within the ice layer may delay the heating rate within the ice phase, however the significant amount of MW power deposition within the water phase may be distributed within the ice phase via conduction (Fig. 8(b)). Note that, the amplitude of the stationary electric field and the MW power absorption within $2L = 0.4$ cm pure ice slab is greater as represented in Fig. 4 and presence of water layer during an intermediate stage causes more destruction between the waves within the ice phase as seen in Fig. 14(b) and (c).

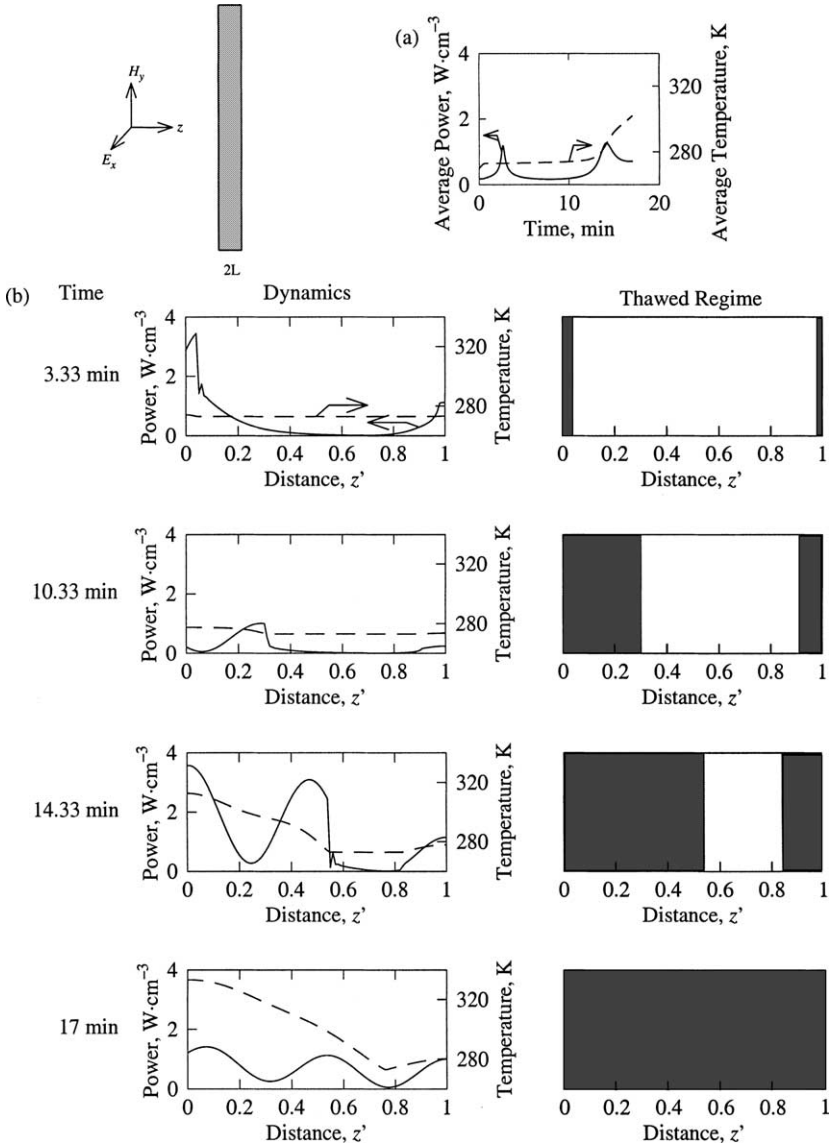

Fig. 12. (a) Average power (—) and average temperature (- - -) vs time; (b) power (—) and temperature (- - -) profiles with thawed regimes (shaded) during microwave thawing of $2L = 1.5$ cm slab exposed to microwaves at the left face. $f = 2450$ MHz, $I_{OL} = 3$ W cm^{-2}, $I_{OR} = 0$. Thawing is seen to proceed from both the faces. Two maxima in average power is observed and average temperature increases rapidly at the later stages due to longer duration of power absorption.

Although amplitudes of waves are smaller in the water region, the maximum power deposition within the water layer is due to the constructive interference ($\delta_{x,l} = 0$) and a greater dielectric loss. During later stages (Fig. 14(c)), the sample consists of 75% of water layer, where the resonance which is however smaller than previous stages, occurs at the opposite face and a very less MW power is being deposited within the ice layer where greater amount of destructive interference still persists.

Although we have assumed the smooth functional representation of dielectric properties within a superficial mushy region for modeling of MW thawing, our analysis for ice–water slabs indicates that the MW power distribution based on the generalized mathematical formulation is identical with the results obtained from finite element based enthalpy formulation during the intermediate and later stages (see Figs. 8(b) and 14(a)–(c)). Similarly, our analysis also explains MW power and heating characteristics for other sample thicknesses which we can see in following discussions. Analysis of MW propagation for $2L = 0.85$ cm sample is shown in Fig. 14(d)–(f). At the initial stage (Fig. 14(d)),

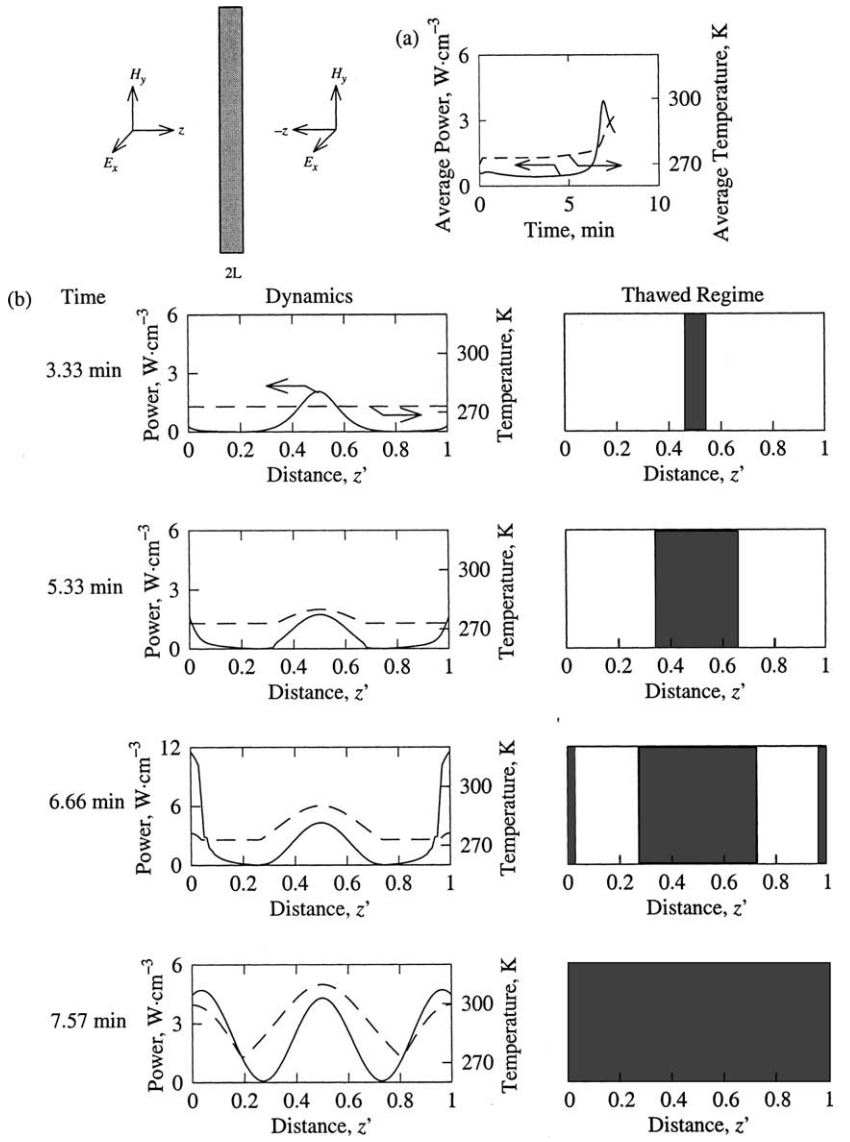

Fig. 13. (a) Average power (—) and average temperature (- - -) vs time; (b) power (—) and temperature (- - -) profiles with thawed regimes (shaded) during microwave thawing of $2L = 1.5$ cm slab exposed to microwaves at both faces. $f = 2450$ MHz, $I_{OL} = I_{OR} = 3$ W cm^{-2}. Thawing is seen to proceed from the center. At a later stage, greater power deposition occur at thin liquid layers attached with both faces. A greater average power at a later stage causes a faster thawing.

thin water layers at the faces are observed and similar to the previous case as seen in Fig. 14(a), the resonance occurs within thin water layers contrasting only one resonating zone for $2L = 0.4$ cm sample. A greater resonance in MW power is observed at the intermediate stage where the entire slab has two thick water layers separated by the central ice region as seen in Fig. 14(e) where many interesting features of wave patterns are also seen. The two water layers enhance amplitudes of the traveling waves within ice layer compared to the initial stage, however these waves are in destructive interference as illustrated by the phase difference, $\delta_{x,l} \geqslant 3.14$, which result in the smaller amplitude of the stationary wave and hence a very small power deposition within the ice layer. The thickness of water layer (15% of the slab thickness) at the exposed face results in greater resonance at this intermediate stage and the magnitude of this resonance is even greater than that at the initial stage. Following our earlier discussion in the previous section (Figs. 8 and 10), we note that the intensity of resonance for $2L = 0.85$ cm sample is considerably greater resulting in $2L = 0.85$ cm to thaw faster

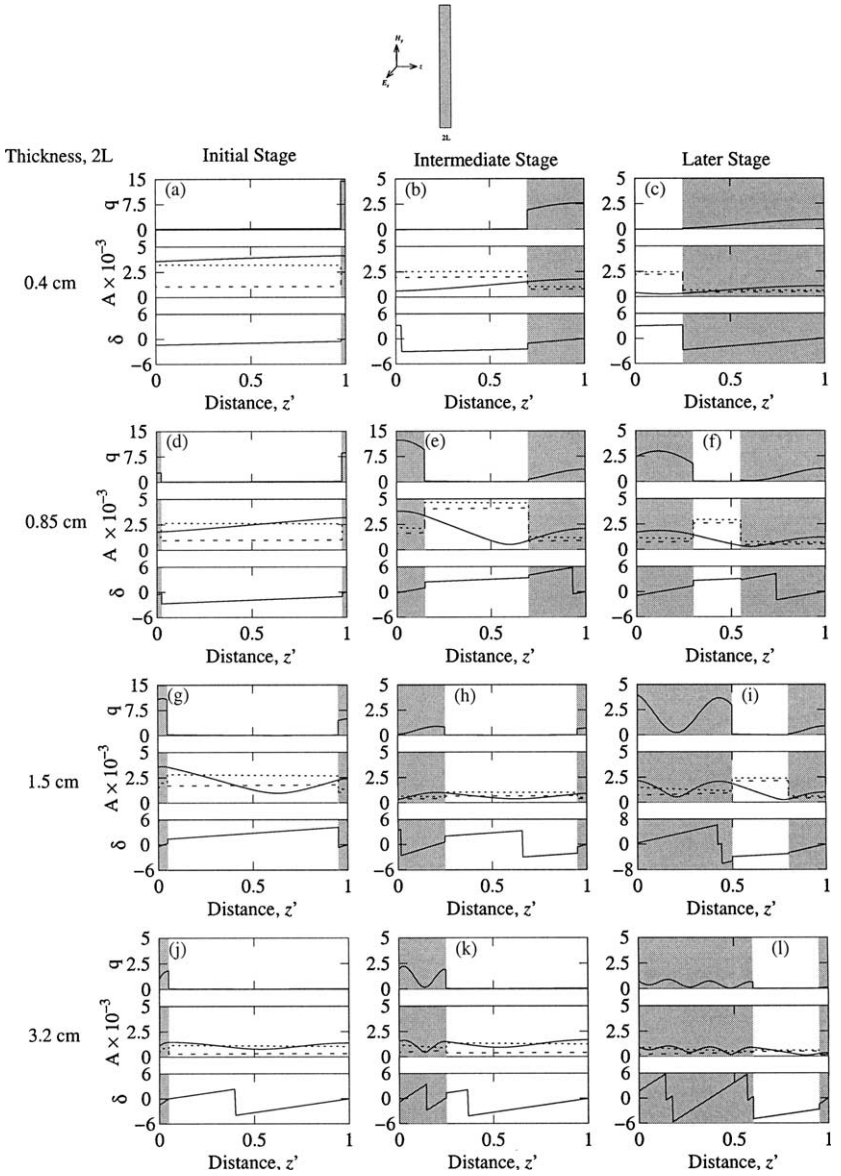

Fig. 14. Power (q, $\mathrm{W\,cm^{-3}}$), amplitudes of waves (A, $\mathrm{V\,m^{-1}}$) and phase difference (δ) distributions (Eqs. (7)–(11)) during initial, intermediate and final stages of thawing for slabs exposed to microwaves at the left face. ($\cdots$) transmitted wave; (- - -) reflected wave; (—) stationary wave. $f = 2450$ MHz, $I_{OL} = 3\ \mathrm{W\,cm^{-2}}$, $I_{OR} = 0$. Greater intensity of resonances occur either at the intermediate or the later stage for $0.85\ \mathrm{cm} \leqslant 2L \leqslant 1.5\ \mathrm{cm}$.

than $2L = 0.4$ cm sample. It is also interesting to note that our simulation studies based on the enthalpy formulation and mixing rules for effective dielectric properties predict the same resonance feature at the intermediate stage as seen in Fig. 10(b). A relatively weaker secondary resonance is also observed at the opposite face (Fig. 14(e)). At a later stage as seen in Fig. 14(f), the resonance and wave patterns are qualitatively similar to that for the intermediate stage with the lowest power deposition within the ice layer, but the resonance near the exposed face shifts towards the middle of water layer which is also in accord with the resonance pattern during 7.33 min as seen in Fig. 10.

As seen in Fig. 14(g), for $2L = 1.5$ cm sample, the spatial wave pattern and the resonance characteristics at the initial stage are qualitatively similar with earlier cases. At the intermediate stage (Fig. 14(h)), the intensity of the resonances is smaller compared to the initial stage, but a relatively strong resonance occurs near the exposed face similar to Fig. 14(e). The stronger reso-

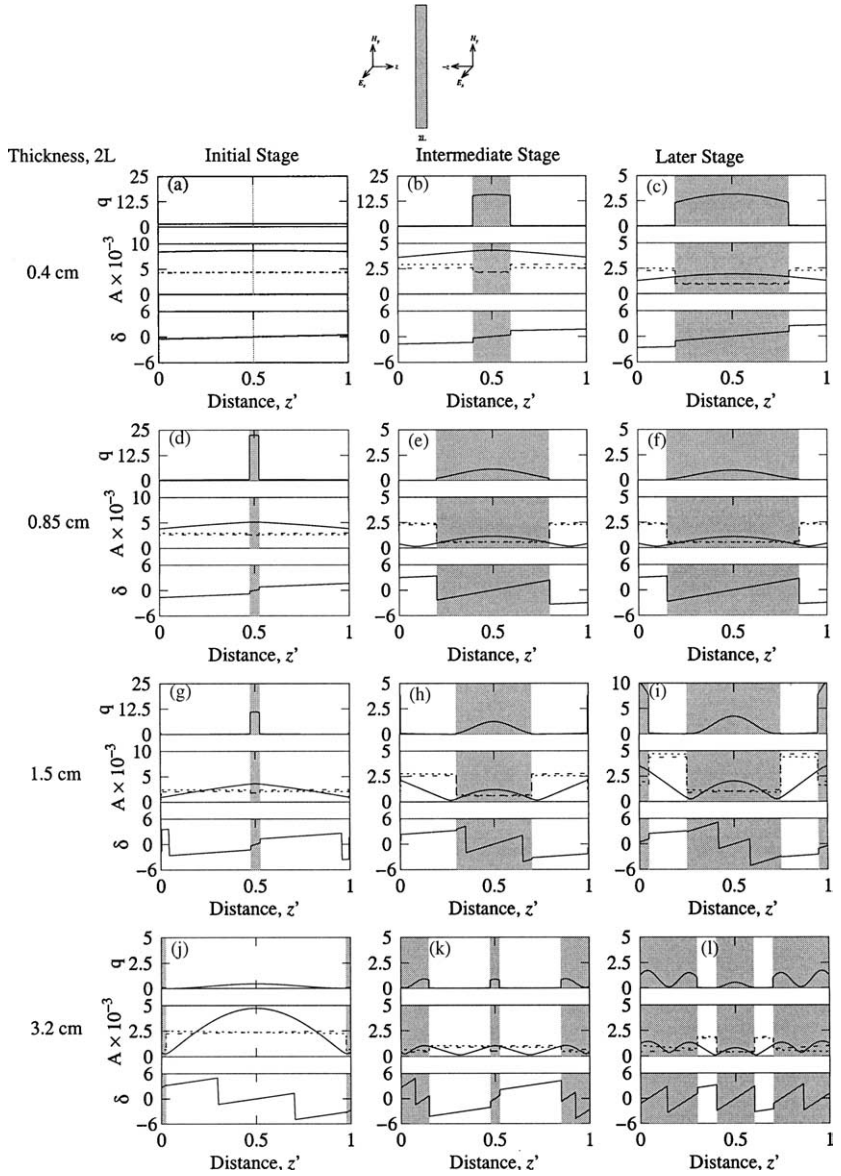

Fig. 15. Power (q, W cm^{-3}), amplitudes of waves (A, v m^{-1}) and phase difference (δ) distributions (Eqs. (7)–(11)) during initial, intermediate and final stages of thawing for slabs exposed to microwaves at both faces. ($\cdots$) transmitted wave; (- - -) reflected wave; (—) stationary wave. $f = 2450$ MHz, $I_{OL} = I_{OR} = 3$ W cm^{-2}. Greater intensity of resonances occur at later stages.

nating zone occurs near the ice–water interface, whereas the secondary resonance is still at the unexposed face. At the later stage (Fig. 14(i)), the water layer near the exposed face is much thicker than that near the unexposed face and two resonating zones occur between the exposed face and the nearest ice–water interface. For a thicker sample ($2L = 3.2$ cm, Fig. 14(j)–(l)), the intensity of resonance is relatively lower at the initial stage, two resonating zones are observed within the water layer at the intermediate stage and multiple resonances with considerably lower intensities at the thick liquid layer near the exposed face are seen at the later stage. The lower penetration of waves within a thicker sample is observed at the later stage where the amplitudes of the traveling waves are considerably lower compared to previous cases.

Fig. 15(a)–(c) illustrate resonance characteristics for $2L = 0.4$ cm slab with MW incident at both faces. A very thin water region at the center during the initial stage of thawing plays no significant influence on MW power absorption at the interface. Amplitudes of the traveling waves are smaller within the finite water region during

the intermediate stage, whereas a resonance at the center of the water region is observed during the intermediate stage (Fig. 15(b)). During a later stage, the qualitative features of resonance is similar to that at the intermediate stage and a lesser MW power absorption at the later stage is seen in Fig. 15(c). For $2L = 0.85$ cm sample, a significant resonance in MW power is observed at the initial stage (Fig. 15(d)) and intensity of resonance occurring always at the center of the water region is decreased as thawing progresses (Fig. 15(e) and (f)). The interesting features for $2L = 0.85$ cm sample with MW incident at the left face are the two water regimes with a resonating zone at both regime occurring at the later stage as seen in Fig. 14(f) which contrast the single resonating zone at the center within a single water layer throughout the thawing process as seen in Fig. 15(f). Note that, the enhanced intensity of resonance due to left side incidence significantly accelerates the thawing process and therefore, the slab with both side MW incidence takes longer time to thaw (see Figs. 10 and 11).

As seen in Fig. 15(g)–(h), for $2L = 1.5$ cm sample, resonating features at initial and intermediate stages are similar to that for $2L = 0.85$ cm sample and a later stage is typically characterized by thin water layers near faces which result in two additional resonances at faces. A greater resonance at faces during the later stage for $2L = 1.5$ cm sample also observed in dynamics of MW thawing simulations as illustrated in Fig. 13(b), accelerates thawing process considerably which resulted in $2L = 1.5$ cm sample to thaw approximately 2 min earlier than $2L = 0.85$ cm sample. For a thicker sample, $2L = 3.2$ cm, the initial stage is characterized by thin layer of water sample at faces where amplitudes of traveling waves are much smaller than rest of the sample, and therefore no resonance occurs within liquid regions as seen Fig. 15(j). At the intermediate stage, two dominating liquid regimes appear from faces with a thin liquid layer at the center (Fig. 15(k)) which result in multiple resonances in MW power occurring at the center of the regime and near the water–ice interface for liquid regions connected with faces. At a later stage, the liquid region connected with faces is thicker where two resonances occur and the central liquid region contains one resonating zone only (Fig. 15(l)).

Before concluding this section, the dynamics associated with various representative thawed regimes and resonance patterns need to be addressed along with a characteristic penetration number, $N_p = 2L/D_p$ where $N_p \gg 1$ denotes an exponential decay of MW power within a sample, $N_p \ll 1$ corresponds to a uniform power resonance throughout the sample and $N_p \approx 1$ results in spatial resonances in power [7,19]. Although the penetration depth, D_p are 25.81 and 2.76 cm for ice and water respectively, we may analyze various thawing scenarios and resonances based on penetration numbers that are calculated using penetration depth in the water phase as water absorbs much greater power than ice. For samples incident from the left face (see Fig. 14), thawing originating from the unexposed face corresponds to $2L \approx 0.4$ cm and $N_p \approx 0.14$ and the thawed regime consists of a single resonating zone occurring at the unexposed face. For $0.14 \leqslant N_p \leqslant 0.30$ (0.4 cm $\leqslant 2L \leqslant 0.85$ cm), thawing occurs from both faces at intermediate stages. It is interesting to note that the resonance, however small, still persists at the unexposed face and a greater resonance occurs at the middle of the thawed regime attached with exposed faces. For $N_p \approx 0.54$, ($2L \approx 1.5$ cm) thawing dynamics are similar to that for $N_p \approx 0.30$, however, as N_p approaches to 0.54, the rate of thawing near the exposed face dominates and the resonating zone within the thawed regime attached with the exposed face approaches to the water–ice interface and at a later stage an additional resonance also occurs just at the exposed face. In sum, for $N_p \leqslant 0.54$, at most two resonances occur within the thawed regime associated with the exposed face and a single resonance with smaller intensity occurs at the unexposed face. As N_p approaches to 1.16 ($2L \to 3.2$ cm), the other thawed regime at the unexposed face is disappeared and only one thawed regime with multiple resonating zones is attached with the exposed face. Note that, intensity of these multiple resonances decays with increasing values of N_p.

For samples, incident from both faces (see Fig. 15), $N_p \leqslant 0.30$, thawing occurs from center with a single resonance at center and the intensity of resonance decreases as N_p approaches to 0.30. For a greater thickness, $0.30 \leqslant N_p \leqslant 0.54$, the initial and intermediate thawed regimes are similar to earlier cases with $N_p \leqslant 0.30$, but at a later stage, additional thawing fronts also appear near both faces where a dramatically greater resonance significantly enhances the thawing process (see Fig. 15(i)). For $N_p \approx 1.16$, thawing regimes occur near both faces initially and additional central thawing regime is seen to appear during intermediate and later stages. Although the central thawed regime contains one single resonating regime, thawed regimes attached with faces contain multiple resonances and similar to Fig. 14, the number of such multiple resonating regions increases with N_p.

Based on our test cases, we find that the presence of central thawed regimes or the thawed regimes attached with unexposed face (for slabs incident at left face only) sometimes enhance the intensity of resonance at the exposed face or both faces which results in higher thawing rates (Figs. 14(e) and 15(i)). Due to presence of multiple thawing fronts, the relationship between stationary wave patterns of ice and water phases is highly non-trivial and a generalized limit of N_p may not be obvious. This is due to the fact that dielectric properties of solid phases of materials vary within a large range and stationary wave patterns in a liquid phase also de-

pend on dielectric properties of neighboring solid phases. Therefore, a modified length scale based on D_p of both solid and liquid phases may be suitable and further analysis on that perspective may be a subject of future work.

3.4. Role of resonance: optimal thawing strategy

To investigate the influence of resonance we have shown the relationship between the thawing time and slab thickness, $2L$ for different MW incidence cases as illustrated in Fig. 16(a) where t_{th_1} and t_{th_2} represent thawing times for one side MW incidence and both side incidence cases respectively. The slab thicknesses are varied upto 5 cm with $N_p = 1.81$ where N_p is obtained based on water phase and a greater difference in thawing time between the two incident cases is at around $2L = 5$ cm sample. It is interesting to note that for all cases the variation of thawing time with slab thicknesses is non-monotonic which contrasts earlier studies on samples with MW incident at one face where a power law between the thawing time and slab thickness was predicted as $t_{th_1} \propto (2L)^n$ as referred in [7,16]. As seen in Fig. 16(a), for samples with MW incident at one face, influence of resonance is attributed around $2L = 0.85$ cm ($N_p = 0.3$) where a local minima of time is observed and t_{th_1} increases rapidly for $2L > 3.2$ cm ($N_p > 1.16$). Greater resonances due to samples with MWs incidence at both faces are observed around $2L = 1.5$ cm ($N_p = 0.54$) where t_{th_2} has a local minima and relatively smaller resonances are also observed around $2L = 3$ cm ($N_p = 1.08$) and $2L = 4$ cm ($N_p = 1.45$). For 0.8 cm $\leqslant 2L \leqslant 0.95$ cm, the samples with one side incidence are influenced greatly by resonances and the samples will thaw relatively slowly when both sources of MWs are on. Based on the time history of thawing for all cases, we find that the presence of resonance causes local minima of thawing time for specific length scales which requires further investigation in order to establish the efficient thawing route with optimal MW power expenditure.

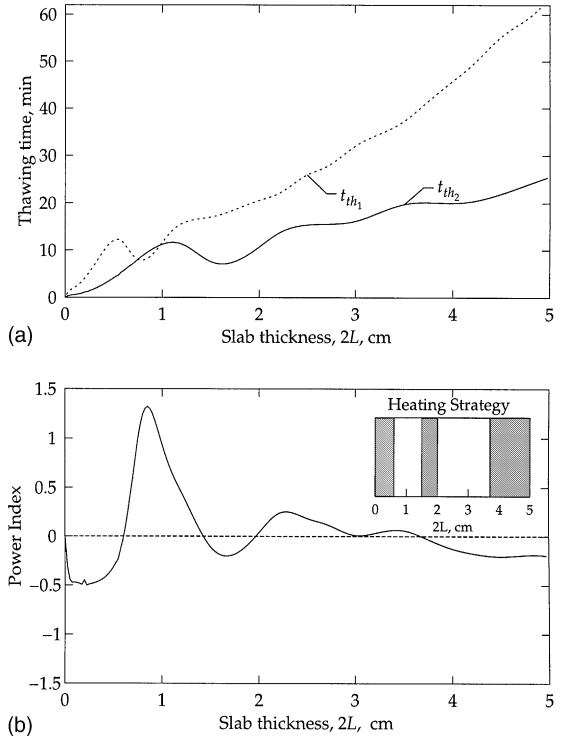

Fig. 16. (a) Thawing time and (b) power index vs slab thickness for samples incident either from the left face or both faces. t_{th_1}, thawing time with left side MW incidence; t_{th_2}, thawing time with both side MW incidence. (—) slabs exposed to microwaves at both faces; (- - -) slabs exposed to microwaves at the left face. $f = 2450$ MHz, for microwaves exposed at both faces; $I_{OL} = I_{OR} = 3$ W cm^{-2}, for microwaves exposed at the left face; $I_{OL} = 3$ W cm^{-2}, $I_{OR} = 0$. The shaded region in the inset denotes the specific sample thicknesses with microwave incidence at both faces where a greater power savings is observed.

To investigate the extent to which power is saved for various MW incidence cases, we define power index, P_i as

$$P_i = \frac{\text{Power expense for both side incidence}}{\text{Power expense for one side incidence}} - 1 = \frac{2I_O t_{th_2}}{I_O t_{th_1}} - 1 = \frac{2t_{th_2}}{t_{th_1}} - 1, \quad (29)$$

where I_O is intensity of MW radiations at each face of samples. $P_i = 0$ indicates that total power expense for both side incidence is identical with power expense for one side incidence case; therefore no power savings or loss for any of the incidence cases, $P_i < 0$ represents total power expense for both side incidence is smaller than power expense for one side incidence and $P_i > 0$ shows the power can be saved with one side MW incidence. Note that $|P_i| \geqslant 1$ indicates that power savings associated with time savings.

Fig. 16(b) illustrates the relationship between P_i and $2L$ (Eq. (29)) where we find that sign of power index varies significantly with $2L$. For $2L \leqslant 0.6$ cm, P_i is negative and $P_i \approx -0.5$ for $2L = 0.3$ cm samples. For 0.6 cm $\leqslant 2L \leqslant 1.2$ cm, P_i is positive which shows that in this region only one side MW incidence is efficient. In addition $P_i = 1.3$ for $2L = 0.9$ cm sample indicates a faster thawing process with both power and time savings. Although for 1.2 cm $\leqslant 2L \leqslant 2$ cm, both side incidence is advantageous, for 2 cm $\leqslant 2L \leqslant 3.5$ cm, one side incidence is preferred and both side incidence is advantageous for $2L > 3.5$ cm samples. An optimal heating strategy based on power index, P_i, is illustrated by the inset of Fig. 16(b) where the shaded regions denote

specific sample thicknesses with MW incidence at both sides and unshaded regions for sample thicknesses with MW incidence at one face only. If a sample thickness falls within a shaded region, we recommend to use MWs incidence at both faces and for unshaded region, one side MWs incidence.

4. Conclusion

We have carried out extensive studies to investigate MW resonances and thawing dynamics for frozen slabs of ice. A generalized mathematical formulation for uniform plane waves has been established for a multilayered/multiphase slab in order to carry out the spatial distribution of MW power and amplitudes of reflected and transmitted waves. MW thawing of ice has been modeled using the enthalpy formulation of the energy balance equation and Maxwell's equations for MW power. The single energy balance equation, consisting of both enthalpy and temperature, is solved for the entire domain and the state of the material is determined from the equilibrium ϕ_l vs T relationships. For pure substances like ice which has discontinuities in the $\phi_l(T)$ curves, a superficial phase change region is assumed around the point of discontinuity. MW thawing dynamics were simulated using Galerkin finite element method.

A preliminary analysis of amplitudes, phase states of reflected and transmitted waves and MW power distributions has been carried out for pure ice and water samples of various thicknesses. We have selected four specific sample thicknesses ($2L = 0.4$, 0.85, 1.5, 3.2 cm) based on our studies for spatial power distributions and resonances within water samples as water has greater dielectric loss. Simulations for ice slabs exposed to microwaves from one face indicate that thawing can occur from the unexposed face for smaller samples and for a relatively larger thickness, a thawing front also appears at the exposed face. We observe a counter-intuitive situation where 0.85 cm slab thaws quicker than 0.4 cm slab, due to occurrence of significantly greater resonance within the thawed regime attached with the exposed face. For greater thicknesses ($2L > 1.5$ cm) thawing occurs primarily from the exposed face with another additional fronts also appearing at the unexposed end during later stages. Consequently, we find that for $2L = 0.85$ cm sample, one side MW incidence gives faster thawing rate than both side MW incidence.

For samples exposed to microwaves from both faces, thawing occurs only from the center for smaller thickness ($2L \leqslant 0.85$ cm) and additional thawing fronts occur at both faces for thicker samples ($2L \geqslant 1.5$ cm). It is interesting to note that $2L = 1.5$ cm sample thaw faster than 0.85 cm sample due to greater resonance occurring at the faces for 1.5 cm sample. Common to one side incidence and both side incidence cases is the greater MW power deposition which is attributed by greater resonance occurring within a secondary thawed regime appearing at later stages for intermediate sample thicknesses. We have also contrasted resonance characteristics between one side and both side exposed cases for specific thicknesses. Based on spatial resonance pattern, either microwave incidence from one face or both faces is preferred.

A detailed analysis on the role of multiple phases in resonance patterns was carried out based on the generalized mathematical analysis to investigate the spatial distribution for phase states and amplitude of waves. This analysis based on the generalized mathematical formulation agrees well with our finite element simulation results for MW power absorptions. Our analysis on resonances for representative thawed regimes clearly explains the occurrence of resonances associated with various traveling and stationary waves. This analysis also clearly demonstrates the occurrence of multiple resonances at later stages.

We have described different thawing trends and resonances which can be broadly classified based on penetration numbers, N_p. However, a generalized thawing tendency and resonances irrespective of material properties need to be further investigated to obtain a generalized classification based on N_p.

A broader perspective on the role of resonance is illustrated by the relationship between thawing time with various slab thicknesses. Thawing times are contrasted for one side and both side exposed cases and we find a non-monotonic trend in variations of thawing times for all cases. Further, we defined 'power index' to quantify power savings in order to highlight optimal thawing strategies. Although our analysis is carried out for a pure slab of ice, we expect similar thawing trends for materials with similar dielectric properties. A scale analysis on a generalized microwave heating/thawing studies is the subject of our ongoing research.

References

[1] K.G. Ayappa, Modeling transport processes during microwave heating: A review, Reviews in Chemical Engineering 13 (1997) 1–69.
[2] K.G. Ayappa, H.T. Davis, E.A. Davis, J. Gordon, Two-dimensional finite element analysis of microwave heating, American Institute of Chemical Engineering Journal 38 (1992) 1577–1592.
[3] T. Basak, K.G. Ayappa, Influence of internal convection during microwave thawing of cylinders, American Institute of Chemical Engineering Journal 47 (2001) 835–850.
[4] T. Basak, K.G. Ayappa, Role of length scale on microwave thawing dynamics in 2D cylinders, International Journal of Heat and Mass Transfer 45 (2002) 4543–4559.

[5] S.A. Barringer, E.A. Davis, J. Gordon, K.G. Ayappa, H.T. Davis, Effect of sample size on microwave heating rate: Oil vs water, American Institute of Chemical Engineering Journal 40 (1994) 1433–1439.
[6] K.G. Ayappa, H.T. Davis, S.A. Barringer, E.A. Davis, Resonant microwave power absorption in slabs and cylinders, American Institute of Chemical Engineering Journal 43 (1997) 615–624.
[7] T. Basak, K.G. Ayappa, Analysis of microwave thawing of slabs with effective heat capacity method, American Institute of Chemical Engineering Journal 43 (1997) 1662–1674.
[8] M. Bhattacharya, T. Basak, K.G. Ayappa, A fixed-grid finite element based enthalpy formulation for generalized phase change problems: role of superficial mushy region, International Journal of Heat and Mass Transfer 45 (2002) 4881–4898.
[9] T. Ohlsson, P.O. Risman, Temperature distribution of microwave heating-spheres and cylinders, Journal of Microwave Power 13 (1978) 303–310.
[10] H. Massaudi, C.H. Durney, P.W. Barber, M.F. Iskander, Electromagnetic absorption in multilayered cylinder models of man, IEEE Transaction on Microwave Theory and Techniques 27 (1979) 825–830.
[11] H. Massaudi, C.H. Durney, C.C. Johnson, A geometrical-optics and an exact solution for internal fields in and energy absorption by a cylindrical model of man irradiated by an electromagnetic plane wave, Radio Science 14 (1979) 35–42.
[12] R. Ruppin, Electromagnetic power deposition in a dielectric cylinder in the presence of a reflecting surface, IEEE Transaction on Microwave Theory and Techniques 27 (1979) 910–914.
[13] C.M. Weil, Absorption characteristics of multilayered sphere models exposed to UHF/microwave radiation, IEEE Transaction on Biomedical Engineering 22 (1975) 468–476.
[14] E.U. Schundler, Microwave drying of ceramic spheres and cylinders, Transactions of the Institution of Chemical Engineers 71 (1993) 622–628.
[15] K.G. Ayappa, Resonant microwave power absorption in slabs, Journal of Microwave Power and Electromagnetic Energy 34 (1999) 33–41.
[16] B.P. Pangrle, K.G. Ayappa, H.T. Davis, E.A. Davis, J. Gordon, Microwave thawing of cylinders, American Institute of Chemical Engineering Journal 37 (1991) 1789–1800.
[17] K.G. Ayappa, H.T. Davis, E.A. Davis, J. Gordon, Analysis of microwave heating of materials with temperature-dependent properties, American Institute of Chemical Engineering Journal 37 (1991) 313–322.
[18] H. Fricke, The complex conductivity of a suspension of stratified particles of spherical or cylindrical form, Journal of Physical Chemistry 59 (1955) 168–174.
[19] T. Basak, Analysis of microwave thawing, Ph.D. thesis, Indian Institute of Science, Bangalore, India, 1999.